Health system learning achieves generalist neuroimaging models

Akhil Kondepudi^{1,2} Akshay Rao¹ Chenhui Zhao^{1,3} Yiwei Lyu^{1,3} Samir Harake¹ Soumyanil Banerjee¹ Rushikesh Joshi^{1,4} Anna-Katharina Meissner⁵ Renly Hou^{1,2} Cheng Jiang^{1,2} Asadur Chowdury¹ Ashok Srinivasan⁶ Brian Athey² Vikas Gulani⁶ Aditya Pandey⁴ Honglak Lee³

Todd Hollon^{1,2,3,4}

¹Machine Learning in Neurosurgery Lab, University of Michigan
 ²University of Michigan Computational
 Medicine and Bioinformatics
 ³University of Michigan Computer Science and Engineering
 ⁴University of Michigan Radiology
 ⁶University of Michigan Radiology

neurovfm.mlins.org

Abstract

Frontier artificial intelligence (AI) models, such as OpenAI's GPT-5 (1) and Meta's DINOv3 (2), have advanced rapidly through training on internet-scale public data, yet such systems lack access to private clinical data. Neuroimaging, in particular, is underrepresented in the public domain due to identifiable facial features within MRI and CT scans, fundamentally restricting model performance in clinical medicine (3). Here, we show that frontier models underperform on neuroimaging tasks and that learning directly from uncurated data generated during routine clinical care at health systems, a paradigm we call health system learning, yields high-performance, generalist neuroimaging models. We introduce NeuroVFM, a visual foundation model trained on 5.24 million clinical MRI and CT volumes using a scalable volumetric joint-embedding predictive architecture. NeuroVFM learns comprehensive representations of brain anatomy and pathology, achieving state-of-the-art performance across multiple clinical tasks, including radiologic diagnosis and report generation. The model exhibits emergent neuroanatomic understanding and interpretable visual grounding of diagnostic findings. When paired with open-source language models through lightweight visual instruction tuning, NeuroVFM generates radiology reports that surpass frontier models in accuracy, clinical triage, and expert preference. Through clinically grounded visual understanding, NeuroVFM reduces hallucinated findings and critical errors, offering safer clinical decision support. These results establish health system learning as a paradigm for building generalist medical AI and provide a scalable framework for clinical foundation models.

Keywords: health system learning, neuroimaging, joint embedding-predictive architectures, artificial intelligence, medical computer vision, foundation models

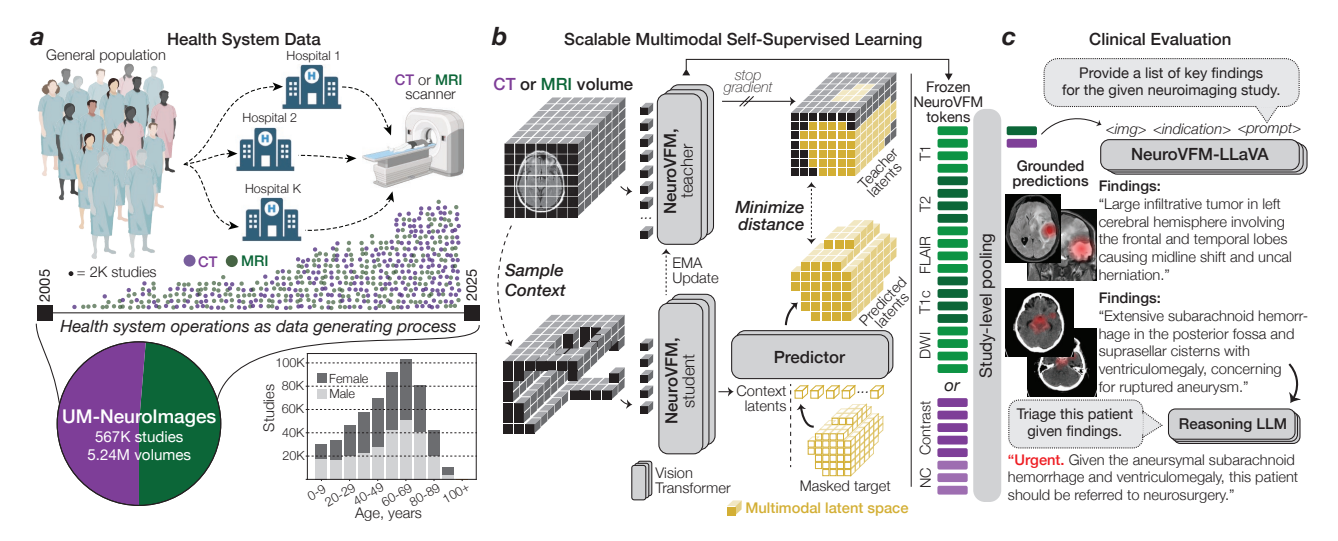


Figure 1 | Overview of Health System Learning with NeuroVFM. a, Health system learning directly models the data generating process of clinical operations at large health systems. The UM-NeuroImages dataset comprises 5.24 million volumes from 566,915 studies, acquired over 20 years at Michigan Medicine. Age and sex distribution are shown below. b, NeuroVFM was trained using Vol-JEPA, a scalable volumetric self-supervised method that learns a unified latent space for CT and MRI. A 3D volume is partitioned into a small context and larger masked target with the background removed. The context is encoded by an online (*student*) 3D vision transformer. A predictor combines context latents with position encodings of the masked target region to predict the masked region latents. Ground truth latents for the masked region are generated by an offline (*teacher*) encoder updated by an exponential moving average, with gradients stopped through the teacher. Training minimizes the distance between the predicted and teacher latents using a smooth L1 loss. c, At inference, NeuroVFM encodes all volumes in a neuroimaging study into latent visual tokens for downstream tasks. The same visual tokens can be used to fine-tune an open-source multimodal language model (i.e., Qwen3-14B, LLaVA-1.5-style) to generate radiology reports. Illustrative findings and corresponding grounded attention maps are shown. The findings can then be passed to a frontier reasoning LLM (i.e., GPT-5-thinking) for interpretation and triage.

Main

Multimodal large language models (MLLMs) derive much of their capability from learning on internet-scale data, enabling these models to approximate the breadth of human experience across language, images, and video. Clinical medicine, however, is underrepresented on the public internet. MLLMs trained exclusively on public data lack access to the rich private information embedded in real-world patient care, which fundamentally limits their performance on clinical tasks. We propose *health system learning* as a new paradigm in which medical foundation models learn directly from uncurated data generated during clinical operations at health systems. By learning in the same complex, nuanced environment in which expert clinicians themselves train, rather than second-hand internet descriptions used by MLLMs, AI models can acquire rich, medical representations grounded in anatomy, pathology, and clinical workflows. MLLMs know the map, health system learners know the territory.

To demonstrate the strength of health system learning, we introduce NeuroVFM, a generalist neuroimaging visual foundation model trained on all clinical MRI and CT studies from a large academic health system. Unlike previous models that rely on data curation, human annotations, or radiology report supervision (4, 5), NeuroVFM is optimized for general neuroimaging through a self-supervised vision-only algorithm called Volumetric Joint-Embedding Predictive Architectures (Vol-JEPA) (6). Our method enforces representation learning across imaging modalities and disease spectra, capturing both global and fine-grained neuroanatomic and pathologic features. Health system learning with Vol-JEPA enables NeuroVFM to achieve state-of-the-art performance, surpassing leading proprietary and open-source frontier models across multiple clinical tasks, including radiologic diagnosis and report generation. NeuroVFM predictions are diagnostically grounded, with pathologic image regions mapped to neurologic diagnoses. When integrated with open-source language models, NeuroVFM acts as a visual understanding module that outperforms GPT-5 and Claude Sonnet 4.5 on neuroimag-

ing interpretation and triage, while reducing hallucinated findings. These results show that NeuroVFM narrows the gap between frontier AI systems and safe clinical deployment.

Learning with Vol-JEPA

To train NeuroVFM, we assembled a multicenter, health system-scale, multimodal dataset called **UM-NeuroImages** (Fig. 1a). The dataset captures real-world neuroimaging studies ordered by physicians across a diverse patient population as part of routine clinical care. We queried Michigan Medicine's picture archiving and communication system for all MRI and CT imaging studies of the brain, head, neck, face, and orbits, yielding 566,915 studies, 5.24 million 3D volumes, and more than 200 million 2D images. UM-NeuroImages is an order of magnitude larger than previous 3D neuroimaging datasets. A clinically informed diagnostic ontology was defined, encompassing 74 MRI and 82 CT diagnoses spanning all major pathologic categories, including neoplastic, traumatic, infectious, and inflammatory disorders. Using a validated AI-based annotation strategy (7), GPT-4.1-mini automatically assigned radiologic diagnoses to each study based on the radiology reports. These labels were not used for Vol-JEPA pretraining and were used solely to train and evaluate supervised diagnostic heads. Detailed dataset characteristics, including sequence types, image resolutions, and diagnosis distributions, are provided in Extended Data Fig. 2.

JEPAs are self-supervised learning methods that, given a context region within a data sample, predict a non-overlapping target region in a learned latent space. JEPA has achieved state-of-the-art performance on image and video data, but has not been applied to volumetric medical images (8–10). We developed Vol-JEPA for volumetric neuroimages to capture invariant semantic information, such as radiologic diagnoses, and spatially equivariant local information, including lesion localization, patient orientation, and neuroanatomy. A critical component of JEPA training is the masking strategy used to define context and target regions. Because neuroimages exhibit intrinsic spatial structure determined by anatomy, we leveraged this property to design a neuroanatomy-informed masking strategy optimized for volumetric learning.

Given an MRI sequence or CT volume, the patient is first segmented as foreground, and the volume is divided into volume tokens (Fig. 1b). A random location within the patient volume is selected as the centroid of a masked block, and additional centroids are sampled until approximately 85% of tokens are masked. The union of these regions forms the Vol-JEPA target, while the remaining tokens define the context (Extended Data Fig. 1). In one configuration, peripheral regions such as the face, scalp, and prefrontal cortex serve as context, and the model, a vision transformer (11), predicts deeper structures including the basal ganglia, brainstem, and occipital lobe. In the inverse configuration, the context consists of deep structures and the target is the periphery. Each minibatch contains an equal mix of both configurations to ensure balanced neuroanatomic learning. Successfully performing this task requires an understanding of anatomic orientation, neuroanatomy, radiographic features, and neurologic disease. Because Vol-JEPA learns through prediction rather than autoencoding or contrastive objectives, it does not require voxel-level augmentations, negative pairs, generative decoders, large batch sizes, or radiology reports. This enables efficient scaling to large, uncurated clinical datasets. A detailed schematic of Vol-JEPA training is shown in Extended Data Fig. 3.

Testing NeuroVFM on diverse neuroimaging tasks

To compare pretraining on health system data with pretraining on public data, we conducted a year-long, multicenter diagnostic study across our health system. All patients consecutively evaluated between June 1, 2023, and May 30, 2024, who underwent a CT or MRI of the head or neck were enrolled without exclusion, yielding a representative sample of real-world clinical imaging. This cohort comprised more than 21,000 head CTs and 29,000 brain MRIs (Supplementary Data Table 1).

NeuroVFM achieved an average AUROC of 92.7 \pm 0.4% across 82 CT diagnostic tasks and 92.5 \pm

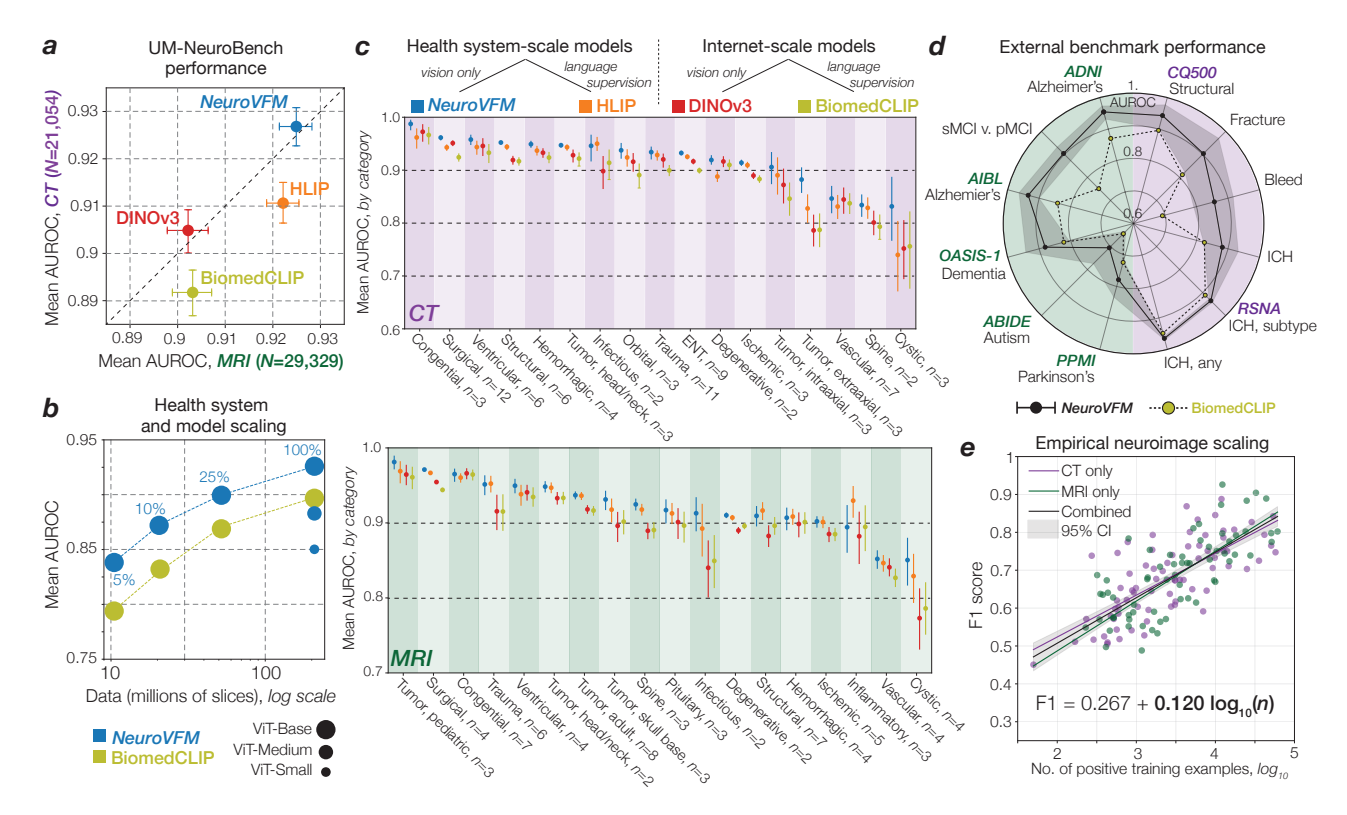


Figure 2 | NeuroVFM results. a, NeuroVFM performance over 82 CT and 74 MRI diagnostic tasks, and compared with both health system-scale (HLIP) and internet-scale (DINOv3, BiomedCLIP) models. NeuroVFM outperforms models trained with language supervision and those trained on public internet data. Results are mean ± 95% CI. b, NeuroVFM exhibits foundation model behavior, with performance scaling across data volume and model size. c, Performance across diagnostic ontologies, such as traumatic, congenital, ischemic lesion, etc. is shown for both CT and MRI. NeuroVFM consistently outperforms other baselines. d, NeuroVFM was tested on CT and MRI-based *external* benchmarks, including Alzheimer's disease, Parkinson's disease, and autism classification, as well as intracranial hemorrhage detection. NeuroVFM outperformed internet-scale models by a wide margin. e, We discovered an empirical log-linear scaling relationship between the number of positive training examples and model performance. This relationship held across at least 4 orders of magnitude, imaging modalities, and models (Extended Data Fig. 4 and 5).

0.4% across 74 MRI diagnostic tasks (Fig. 2a). We compared NeuroVFM with three state-of-the-art models: the health system-trained HLIP model (13) and two internet-scale baselines, DINOv3 and BiomedCLIP. For each model, we trained an attentive pooling classifier on frozen embeddings from UM-NeuroImages. NeuroVFM outperformed all baselines for both CT and MRI diagnosis, demonstrating the value of scalable self-supervised learning and health system-scale pretraining. Its performance was comparable to or exceeded that of established diagnostic tools used by expert neuroradiologists such as the ASPECTS score for ischemic stroke (14) and the T2-FLAIR mismatch sign for diffuse glioma (15) (Extended Data Fig. 4 and 5).

We found that NeuroVFM exhibits the hallmark properties of foundation models, with performance scaling predictably across both data volume and model size (Fig. 2b) (16). Empirically, we observed a non-saturating log-linear relationship between the number of positive diagnostic examples and performance metrics (Fig. 2e). NeuroVFM maintained stable performance across MRI manufacturers, magnetic field strengths, demographic subgroups, and medical centers (Extended Data Fig. 6). We further evaluated the model on multiple public neuroimaging benchmarks, including brain age estimation, dementia and autism classification, and intracranial hemorrhage detection. Across nearly all tasks, NeuroVFM outperformed internet-scale baselines by a wide margin (Fig. 2d, Extended Data Fig. 7).

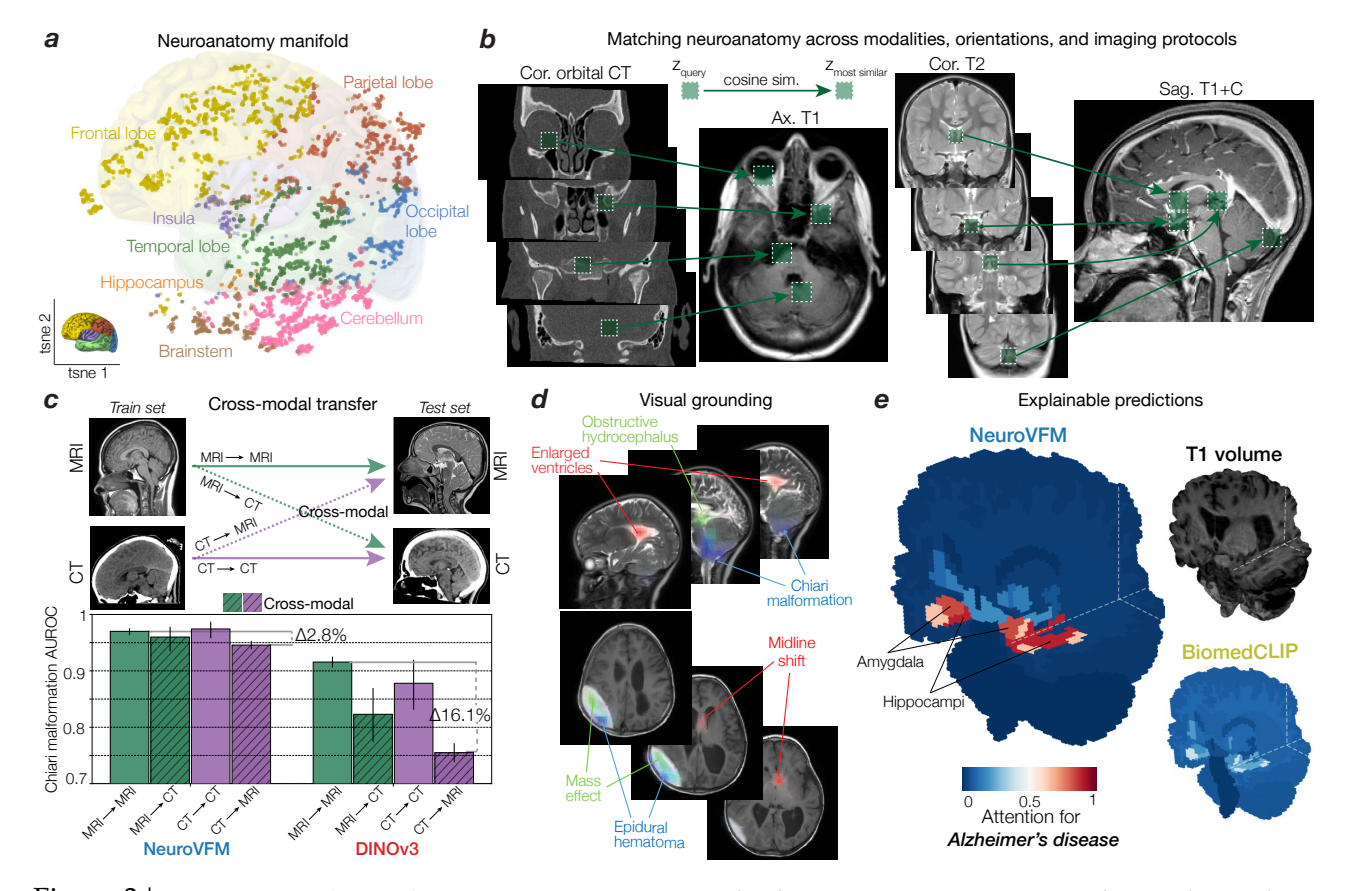


Figure 3 | NeuroVFM understands neuroimaging. a, A T1-weighted MRI sequence was segmented using the SynthSeg model (12). Tokens were embedded into the learned NeuroVFM representation space and plotted using t-SNE. Each token is plotted (dots) and colored according to the segmentation map. NeuroVFM organized visual tokens into a latent neuroanatomic manifold that accurately encodes both spatial and semantic features. b, NeuroVFM implicitly matches and registers anatomic regions from different modalities, patient orientations, and imaging protocols. c, As a multimodal model with a shared representation space between CT and MRI, NeuroVFM understands pathology across these modalities. An MRI classifier for Chiari malformations, for example, transfers to CT, and vice versa. DINOv3 representations do not exhibit consistent cross-modal performance. Additional cross-modal transfer results are in Extended Data Fig. 4 and 5. d, NeuroVFM predictions are grounded, with diagnostic attention placed on pathologic regions. A patient with a history of obstructive hydrocephalus and Chiari malformation is above, and below is a patient with an epidural hematoma causing mass effect and midline shift. e, NeuroVFM also produced explainable classifier predictions. A NeuroVFM-based Alzheimer's disease classifier attends to mesial temporal structures, regions most implicated in disease progression.

Emergent neuroimage understanding

Health system learning with Vol-JEPA gave rise to emergent abilities: clinically meaningful behaviors that were not explicitly supervised during training. Without segmentation or label supervision, NeuroVFM organized visual tokens into a latent neuroanatomic manifold that accurately encodes both spatial and semantic features of brain structures (Fig. 3a). Token-level encoding allows the model to match anatomic regions and pathologies across modalities, orientations, and imaging protocols, effectively performing zero-shot semantic matching (Fig. 3b). Similar to how token matching emerges in frontier models trained on natural images such as DINOv3, we observe analogous behavior in NeuroVFM. For example, the model recognizes that the pineal gland on coronal T2-weighted imaging corresponds to the same structure on sagittal T1-weighted post-contrast imaging. These results imply that NeuroVFM has learned an *implicit brain atlas of human neuroanatomy*. This emergent capability extends to zero-shot diagnostic transfer between MRI and CT, a property not observed in DINOv3 embeddings (Fig. 3c). A classifier trained on CTs to detect Chiari malformation, midline shift, or ventriculomegaly transfers to MRIs without additional training (Extended Data Fig. 4, 5). By learning invariant disease representations that decouple pathology from modality-specific features, NeuroVFM

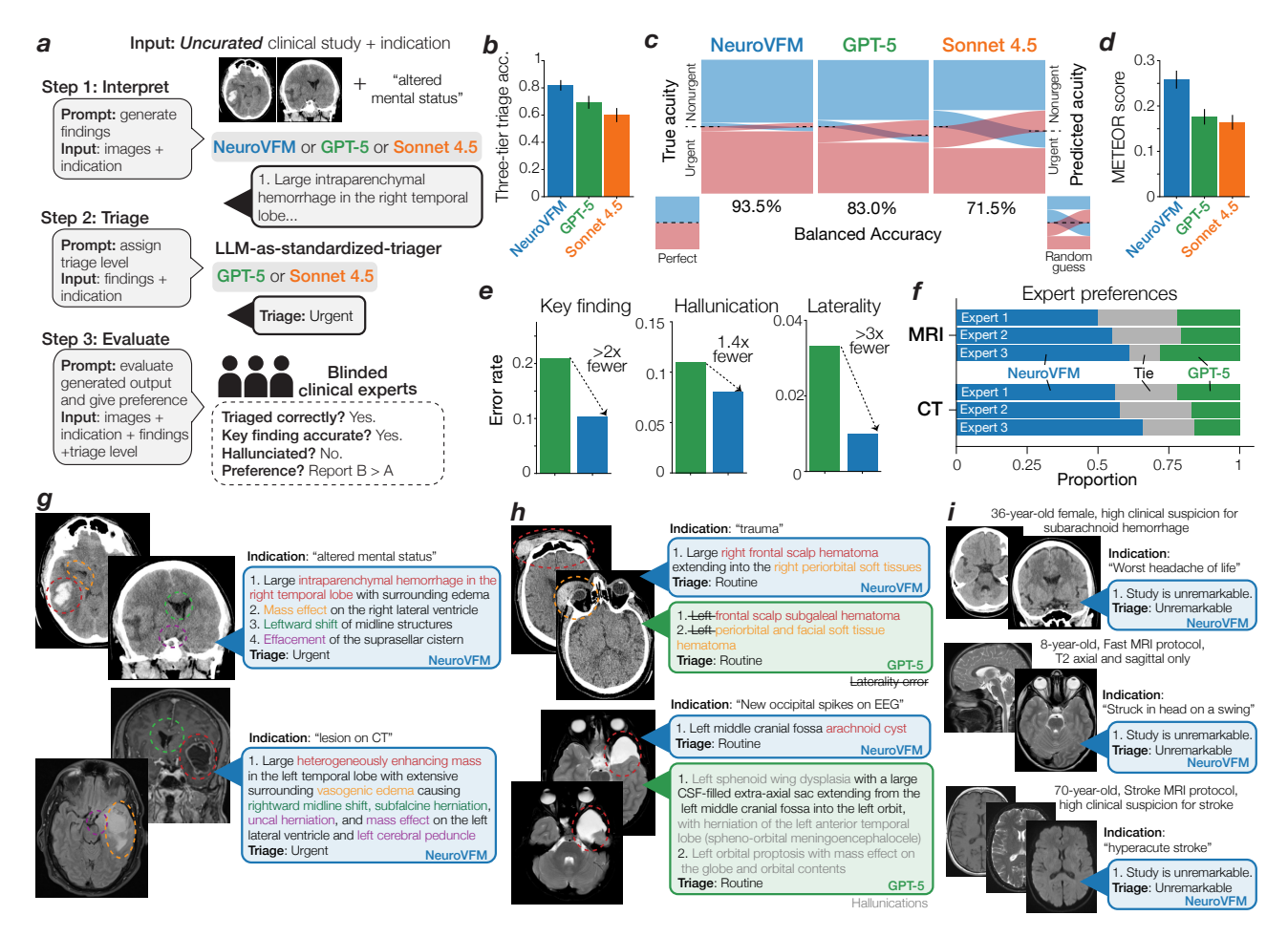


Figure 4 | Triage report generation results. a, Overview of the study design and workflow for report generation and triage. (Step 1) A generative multimodal model, such as NeuroVFM-LLaVa or GPT-5, is prompted to generate image key findings. (Step 2) An LLM, GPT-5 or Claude Sonnet 4.5, is then used as a standardized judge to triage the study based on the findings generated in Step 1. (Step 3) *Blinded* clinical experts then evaluate whether the study was triaged correctly, the quality of the generated reports, and which report they prefer. NeuroVFM outperformed the other frontier models on overall triage performance (b), urgent findings generation (c), and all natural language processing metrics (d and Extended Data Fig. 9). e, Blinded clinical experts noted that NeuroVFM was more likely to generate correct key findings, less likely to hallucinate, and much less likely to make a laterality error compared to GPT-5. f, Clinical experts also preferred NeuroVFM reports more than 2:1 over GPT-5 reports. g-i, Illustrative examples of urgent, routine, and unremarkable head CTs and brain MRIs in the expert annotated testing set.

inherits robustness to variations in scanner hardware, protocols, and sites (Extended Data Fig. 6).

We define diagnostic grounding as the model's ability to localize image regions that causally support a diagnostic prediction. To evaluate grounding, we used an attention-based multiple instance learning (AB-MIL) framework (see Methods) (17). NeuroVFM accurately localized pathologic regions and mapped them to corresponding radiologic diagnoses (Fig. 3d). For example, NeuroVFM correctly attends to and assigns the diagnostic labels to a patient with an epidural hematoma causing mass effect and midline shift. This comprehensive visual understanding extends across diverse pathologies, as illustrated in Extended Data Fig. 8. NeuroVFM also produced explainable classifier predictions for complex diseases such as Alzheimer's, attending to mesial temporal structures, including the hippocampus and amygdala, known to be implicated in disease progression (Fig. 3e) (18). These results parallel the emergent abilities seen in frontier foundation models (19), suggesting that health-system-scale self-supervised training can yield qualitatively new capabilities in medical AI.

NeuroVFM outperforms frontier models for report generation

Frontier models such as GPT-5 and Claude Sonnet 4.5 are generative vision-language systems trained at internet scale on a vast corpus of public medical images and text. We tested whether NeuroVFM, when paired with an open-source language model trained only with autoregressive next-word prediction, could outperform these frontier models on the task of generating radiology reports for clinical triage. Triage is a high-yield application for AI, benefiting patients, radiologists, and clinicians through increased efficiency and early prioritization of urgent findings (20, 21). In this task, the model must generate itemized reports for *real-world*, *uncurated*, *clinical*, *neuroimaging studies* that accurately describe all key pathologic findings to classify each study into one of three clinical categories: unremarkable, routine, or urgent (Fig. 4a).

The frozen NeuroVFM model was paired with the open-source language model Qwen3 in a standard LLaVA-1.5-style visual instruction tuning framework to evaluate the quality of NeuroVFM's learned representations for report generation (Fig. 4) (22, 23). Our goal was not to optimize for report generation performance but to assess the feasibility of training a simple generative model directly from NeuroVFM embeddings. The vision-language model was trained using standard supervised fine-tuning on the UM-NeuroImages dataset to generate all key pathologic findings (Extended Data Fig. 9). We used frontier reasoning models GPT-5 and Claude Sonnet 4.5 as baselines, prompting each to generate key findings (Supplementary Data Fig. 5). A fixed prompt and language model (GPT-5 or Sonnet 4.5) were then used as standardized judges to assign triage levels based on the generated reports, providing a standardized and model-agnostic evaluation protocol (Supplementary Data Fig. 6). All models were tested on 300 expert-selected CT and MRI studies, balanced across modality and triage level.

NeuroVFM outperformed GPT-5 and Claude Sonnet 4.5 on both three-tier triage accuracy and detection of urgent findings (Fig. 4b, c). When compared with ground-truth radiology reports, NeuroVFM-generated findings achieved higher scores across all natural language evaluation metrics, including METEOR and ROUGE (Fig. 4d and Extended Data Fig. 9). In blinded expert evaluation, the key finding error rate of NeuroVFM-generated reports was roughly half that of GPT-5 (approximately 10% versus 20%), with substantially fewer hallucinations and laterality errors. An international cohort of three blinded clinical experts preferred NeuroVFM-generated reports more than two to one over GPT-5-generated reports with high inter-rater concordance (Fig. 4f; Fleiss' $\kappa = 0.718$).

Figure 4g-i shows representative NeuroVFM-generated reports across urgent, routine, and unremarkable triage levels. NeuroVFM accurately identified large mass lesions, including intraparenchymal hematomas and infiltrative tumors, and recognized associated findings such as midline shift, effacement of the basal cisterns, and brain herniation to determine lesion severity. The model also distinguished intracranial from extracranial hematomas, such as scalp hematomas, an essential distinction for triaging traumatic brain injury. NeuroVFM correctly identified non-urgent findings such as arachnoid cysts, even when producing mild mass effect, and consistently triaged unremarkable CT and MRI studies across imaging protocols and age groups, including those with high-risk clinical indications such as "worst headache of life" or "acute stroke." We observed that both NeuroVFM and GPT-5 appropriately used the clinical indication to improve triage performance, whereas Claude Sonnet 4.5 struggled when given images alone (Extended Data Fig. 9). Examples spanning the full range of pathologies encountered in routine clinical practice are shown in Extended Data Fig. 10.

Discussion

Health systems are knowledge bases and data engines that capture the collective experience of public health and clinical medicine. Here, we demonstrate that directly experiencing the clinical world through health system learning achieves high-performance neuroimaging foundation models. These

task-agnostic vision models, pretrained on large and diverse clinical datasets, provide robust and transferable representations for downstream tasks. By integrating domain-specific intelligence learned from private clinical data with general-purpose reasoning, health system learning and NeuroVFM provides a roadmap towards AI systems that interpret and act on clinical information with subspecialist depth, expert reliability, and safe deployment.

Frontier models benefit from the vastness of publicly available information; however, this breadth limits their depth in technical domains, such as medicine (24). Internet data rarely reflects the complexity and diversity of real-world clinical imaging, where disease manifestations, acquisition protocols, and patient anatomy can vary widely. Health system learning represents a fundamentally different paradigm (25, 26). Rather than learning from descriptions of the clinical world or curated hand-selected patient examples, health system learners, like NeuroVFM, experience the world itself, modeling the raw signatures of diseases embedded in unfiltered clinical data. World models have gained attention as a strategy to address the limitations of sequence modeling and reinforcement learning (27–29). NeuroVFM shows that intelligence can emerge from observing clinical practice itself.

Our long-term vision for NeuroVFM is to complement frontier models, not replace them in medicine. Agentic AI systems, including GPT-5 and Claude Sonnet 4.5, have integrated tool use to improve performance in specific domains, such as mathematics, science, and medicine (30–32). We foresee NeuroVFM and other health system models being integrated into agentic AI systems as external modules that provide a grounded understanding of clinical data. Frontier models will be able to reason over structured, clinically calibrated outputs from NeuroVFM, reducing failure modes and providing an auditable substrate for action. We believe expert-level performance across most cognitively complex domains will require the integration of domain-specific modules into general-purpose AI models.

Limitations and directions for future research include the need to integrate temporal and additional multimodal data streams, including pathology, genomics, and longitudinal clinical outcomes, to construct unified representations of disease progression. While the present study focuses on neuroimaging, the unified Vol-JEPA architecture is inherently extensible to other medical imaging modalities and body parts. Finally, while NeuroVFM exhibits emergent interpretability, translating these insights into actionable clinical interfaces will require new methods for human–AI collaboration, uncertainty quantification, and prospective evaluation in clinical workflows.

In summary, NeuroVFM demonstrates that generalist medical intelligence can be built from the health system itself. Learning directly from health system data yields representations that translate to diagnosis, triage, and report generation. We provide a scalable blueprint towards the development of medical foundation models that will be transformative in 21st century healthcare.

Methods

Principles of Health System Learning

We view health system learning as the environment within which generalist medical foundation models can emerge (33). To clarify the concept and differentiate it from existing foundation model training methods, such as internet-scale or life science training, we elaborate on several principles that define health system learning.

- 1) Directly learning the clinical world: Models should learn from data generated during routine patient care with no or minimal data processing or curation, experiencing the breadth and complexity of clinical medicine. This ensures robustness, realism, and coverage of clinically important edge cases.
- 2) *Scalable training*: Health system datasets require scalable supervision. Self-supervised learning objectives, including predictive, contrastive, and autoencoding objectives, are the current preferred strategy. However, other methods, such as semi-supervision or energy-based objectives, are candidates for scalable health system learning.
- 3) Clinical grounded representations: Medical foundation models trained through health system learning should internalize anatomy, pathology, and physiologic variation that supports accurate diagnosis, cross-modal reasoning, and interpretable grounding, thereby reflecting the epistemic structure of clinical expertise.
- 4) *Multimodal medical learning*: Health system data are multimodal representations of a single underlying object: the patient. Any single modality is a partial and incomplete view of the patient. Multimodal models can achieve more complete representations and better disentangle explanatory features across modalities
- 5) *Integration with agentic and multimodal AI systems*: Health system learning is inherently modular. The resulting domain-specific foundation models can serve as expert visual or multimodal modules within larger agentic systems. This complements general-purpose models, enabling clinically safe, domain-aligned reasoning at scale.

UM-NeuroImages Dataset

Radiology studies at large academic medical centers are stored in picture archiving and communication systems (PACS). We queried the University of Michigan PACS via a SQL-based interface (Sectra Data Warehouse) for neuroimaging studies that satisfy: 1) an acquisition date prior to June 1, 2023; 2) an examination of body part(s) including the head, brain, orbits, face, or neck; and 3) a modality of MRI or CT. The specific SQL query parameters are in Supplementary Data Figure 1.

The initial query yielded 645,989 unique studies. After removing non-image/corrupted entries and embedded non-DICOM files, the final cohort comprised 566,915 studies (275,981 MRI studies and 290,934 CT studies). Series counts were 3,647,950 MRIs and 1,591,629 CTs, for a total of 5,239,579. Descriptive characteristics are in Extended Data Fig. 2a-d. For 444,188 studies with paired radiology reports (MRI, 218,882; CT, 224,306), we used GPT-4.1-mini to extract diagnoses and summarized findings, following prior report-parsing work (20, 34–36). We randomly held out approximately 1,000 MRI and 1,000 CT studies as a validation set for model selection. The test cohort is prospective and temporally held-out, including studies from June 1, 2023, through May 31, 2024.

Series Preprocessing

To ingest the full breadth of health system data without manual curation, we applied an automated pipeline to standardize intensities and dimensions. Series were resampled to $1 \times 1 \times 4$ mm (4 mm along the acquisition axis from DICOM) and saved as 8-bit. MRI intensities were clipped to the 0.5-99.5th percentile before quantization. CT volumes yielded three windows: brain (width=80, level=40; 8-bit),

subdural/blood (width=200, level=80; 4-bit), and bone (width=2800, level=600; 4-bit). 4-bit windows reduced storage while preserving contrast for key pathologies. Background masks were derived via Otsu and Hounsfield thresholding for MRI and CT, respectively. During training, volumes were cast to float, scaled to [0,1], and mean-normalized using statistics derived from the training set. Extended Data Fig. 1b summarizes this pipeline.

NeuroVFM Training with Vol-JEPA

The core training objective for NeuroVFM was large-scale self-supervision, applied at the individual volume level, across the entire UM-NeuroImages dataset. NeuroVFM employs a joint-embedding predictive architecture (JEPA) to optimize a masked modeling objective directly in the representation space. First, input volumes are tokenized into non-overlapping 3D patches of $4\times16\times16$ voxels. Each 3D volume is then partitioned into a small, visible context region, x, and larger, masked target region, y. The tokenized context region is processed by a trainable student encoder, E_{θ} . The resulting context representations $E_{\theta}(x)$, along with positional information of the masked target patches, are then fed to a predictor module, P_{ϕ} , which generates predictions for the representations of these target patches. The complete set of tokens from the input volume (representing both context and target regions) is processed by a teacher encoder, whose weights E_{θ} are updated as an exponential moving average (EMA) of the student encoder's weights after each step and are not directly optimized by gradient descent. The training objective minimizes the difference between the predicted representations of the target patches and those generated by the teacher network for the same target patches. This is formulated as:

$$\operatorname{minimize}_{\theta, \varphi, \Delta_{y}} \| P_{\varphi}(\Delta_{y}, E_{\theta}(x)) - \operatorname{sg}(E_{\bar{\theta}}(y)) \|_{\operatorname{smooth L1}}, \quad (8)$$

where Δ_y is a set of learnable tokens that represents the masked target patches and $sg(\cdot)$ denotes a stop-gradient operation. This representation-level objective is computationally efficient and encourages the learning of semantic features without requiring explicit voxel-level augmentations or decoding.

Volumetric-JEPA (Vol-JEPA) extends the principles of I-JEPA (8) and V-JEPA (10) for self-supervision to volumetric neuroimages, predicting representations of masked 3D target patches based on visible 3D context patches. This encourages the model to learn the shared anatomy of the brain, head, and neck. The masking strategy was foreground-focused: context and target patches were sampled exclusively from the pre-computed head mask. Masking was performed in two ways: (1) multiple large crops are sampled, with their union forming the masked target, and (2) a small crop is sampled as context, with the complement being the target. A random subset of context patches is then dropped, serving as additional target patches to predict. Unlike approaches that truncate sequences within a mini-batch to a uniform length, our implementation leverages FlashAttention-2 (37) to directly encode variable-length sequences of context and target patches derived from input volumes. To ensure robustness to varying patient orientations, we applied random axis permutations and flips to each volume, using the same transform for both student and teacher inputs. A hyperparameter search indicated optimal context region sampling ratios (from the total patches within a given crop) of 25% for MR volumes and 20% for CT volumes, with a patch dropout rate of 20%. An overview of this masking strategy can be found in Extended Data Fig. 3a.

During training, volumes were truncated along each axis to a maximum of 20 patches to bound the token count per crop. At inference, the same encoder was applied to the entire volume without truncation, leveraging its ability to handle variable-length token sequences. For CT scans, which are typically viewed with multiple windowing presets (e.g., brain, subdural, bone), we implemented a weighted sampling strategy during training. For pretraining, one of these three CT window settings

was randomly selected and applied with probabilities of 0.7 (brain), 0.15 (subdural), and 0.15 (bone), and all windows were used during inference. Full training details are in Supplementary Data Table 6.

Evaluating diagnostic grounding with multiple instance learning

Most visual grounding evaluation requires an object detection module to output a bounding box around an image region given a label or text prompt. This is not feasible for the current study because there are no object detection datasets or models sufficiently powerful to evaluate neuroimage grounding on the scale and complexity of UM-NeuroImages. Because most neurologic pathologies are spatially small relative to the full study, study-level labels provide only weak supervision. We leveraged an attention-based multiple instance learning (AB-MIL) framework to assess neuroimage grounding (17). AB-MIL is known to assign high attention to diagnostic regions in medical images (38). Unfortunately, the standard AB-MIL framework, with its 'aggregate-then-classify' design, cannot resolve a critical grounding ambiguity: it is unable to disentangle a patch's importance, where the model looks, from its directional contribution, why it is considered positive or negative evidence.

We address this gap with a pooling operation that reverses the standard order to a 'classify-then-aggregate' model. For a task with K classes and a bag of N instances, we first compute classification logits for each instance i using a multilayer perceptron (MLP), ψ_p . A separate attention MLP, ψ_m , generates K class-specific attention scores per instance. For each class, these scores are normalized with a softmax across instances to obtain class-specific attention weights. The final bag-level logits, p(x), are the sum of the element-wise product of the per-instance logits and their corresponding attention weights:

$$p(x) = \sum_{i=1}^{N} \alpha_i \circ \psi_p(f(x_i))$$

Here, $f(x_i)$ is the frozen feature vector for instance i, α_i is the vector of class-specific attention weights, and \circ denotes the Hadamard product. This formulation yields interpretable, label-specific attention maps that reflect both the importance and directional contribution of each region to the diagnostic decision, providing a scalable means of evaluating grounding without region-level annotations.

Comparison to Foundation Model Baselines

We evaluated NeuroVFM against two families of baselines: (1) Internet-scale pretrained encoders, and (2) methods directly trained on UM-NeuroImages. All backbones were frozen and evaluated with the same study-level attentive probe and data splits. Full architecture details, training hyperparameters, and evaluation configurations can be found in Supplementary Data Table 6 and our GitHub repository. A schematic of the study-level pooling strategies can be found in Extended Data Fig. 1e.

Internet-scale pretrained encoders

We chose two baselines representative of the dominant Internet-scale paradigms:

- Natural image self-supervision, **DINOv3** (2): ViT-B/16 pretrained on 1.7 billion natural images (HuggingFace, 'facebook/dinov3-vitb16-pretrain-lvd1689m')
- Medical image-text alignment, BiomedCLIP (39): ViT-B/16 pretrained on 15 million image-caption pairs scraped from PubMed (HuggingFace, 'microsoft/BiomedCLIP-PubMedBERT_256-vit_base_patch16_224')

For 2D encoders, 3D volumes were processed slice-wise according to the model's respective preprocessing pipeline (e.g., DINOv3 necessitates resizing to 224 × 224 and normalizing with ImageNet mean/std), with slice-level features aggregated to produce study-level predictions.

Methods trained on UM-NeuroImages

To provide a controlled comparison of representation learning methods, we trained key architectures on our UM-NeuroImages dataset. For comparison to vision-only self-supervision strategies, we benchmarked against a 3D **Masked Autoencoder** (VideoMAE) (40) with an 85% foreground-aware masking ratio, and **DINOv2** model (41) trained on 2D neuroimaging slices derived from UM-NeuroImages volumes. The DINOv2 features were aggregated in a similar fashion to the pretrained 2D vision encoders. For vision-language alignment comparison, we trained **HLIP** (13), a state-of-the-art 3D medical vision-language model, on our 444,188 study-report pairs and evaluated its study image encoder. HLIP training minibatches were balanced across MRI and CT studies, and the CLIP objective was computed within each modality to prevent trivial cross-modality discrimination.

Diagnostic Evaluation of NeuroVFM

The UM-NeuroImages dataset contains two decades of clinical neuroimaging data from a large academic health system, spanning a broad spectrum of neurological presentations. To evaluate *imaging-only* diagnostic ability, we evaluated NeuroVFM on a prospective, temporally held-out test cohort beginning immediately after the retrospective window. Labels were derived from radiology reports using a LLM extraction pipeline, with a subset manually verified by clinical experts. We defined a clinically organized ontology of 74 MRI and 82 CT diagnoses (Extended Data Fig. 2h). Encoders were frozen, and modality-specific attentive probes were trained for multi-label prediction using class-weighted binary cross-entropy. Hyperparameters and class-specific thresholds were selected on the validation set. We report per-class AUROC, balanced accuracy, sensitivity, and specificity on the test cohort, with 95% CIs from study-level bootstrap resampling (10,000 replicates). Full results are provided in Supplementary Data Table 2 and 3.

Data, model, and modality scaling

We studied performance along data scale, model capacity, and modality with resource-normalized protocols. For modality, we held the optimization budget fixed at ~510K training steps and compared (i) a single multimodal model vs. (ii) two unimodal models (one MRI, one CT) trained separately. For data and model scaling, we varied (a) the fraction of UM-NeuroImages (5%, 10%, 25%), and (b) the encoder size (ViT-Small, ViT-Medium, ViT-Base). Larger backbones (e.g., ViT-Large) were left to future work due to computationally prohibitive hyperparameter search.

Label efficiency

We quantified how per–task performance scales with the amount of supervision. For each diagnostic class c and modality $m \in \{\text{CT}, \text{MRI}\}$, we calibrated model probabilities on the validation set using Platt scaling and computed F1 on the held-out test set. We excluded classes with fewer than 30 training positives (n_{pos}) and 10 testing positives. We fit a simple linear model of F1 vs. $\log_{10}(n_{\text{pos}})$ via OLS with HC3 SEs. Modality fixed effects and interactions assessed CT vs. MRI differences. Encoder comparisons (NeuroVFM vs. HLIP, DINOv3, and BiomedCLIP) used ANCOVA to test slope equality. If interaction terms were non-significant, a shared slope was used, otherwise encoder-specific slopes were retained. Label-equivalence was reported as the fold-increase in positives a baseline requires to match NeuroVFM at a fixed F1, with 95% CIs from 10,000 bootstrap replicates over classes.

NeuroVFM on External Public Benchmarks

To assess the out-of-distribution generalization, we evaluated frozen NeuroVFM performance on eight public neuroimaging benchmarks. For all tasks, we trained an attentive probe without updating the encoder. Within each dataset, we held out 20% of subjects as a stratified test set. On the remaining 80%, we performed 8-fold iterative stratified cross-validation to select probe hyperparameters. The 8 probes trained on the cross-validation folds were then used to generate logits on the held-out test set, which were averaged per study to form the final ensemble. All reported metrics include 95%

subject-level percentile CIs (10,000 bootstrap replicates). This approach rigorously tests the quality of the learned representations and, through the probe's attention weights, allows for the identification of class-discriminative tokens for each task.

External MRI benchmarks

We evaluated NeuroVFM on six public MRI datasets, spanning a range of neurological and psychiatric conditions. On the multi-site **OpenBHB** dataset (42), we benchmarked brain age regression to test for fine-grained anatomical representation. For dementia-related tasks, we utilized the ADNI dataset (43) to perform CN vs. Alzheimer's Disease (AD) classification and to distinguish progressive from stable Mild Cognitive Impairment (sMCI vs. pMCI), with a 20% stratified test set held out within ADNI. We then evaluated the ADNI-trained AD classifier externally on the OASIS-1 (44) and AIBL (45) datasets, applying the frozen probe without further fine-tuning to distinguish cognitively normal individuals (CDR = 0) from those with dementia (CDR \geqslant 1). We further evaluated diagnostic classification on several consortium datasets: differentiating individuals with Autism Spectrum Disorder from typically developing controls on the **ABIDE** dataset (46) and Parkinson's Disease from healthy controls on the **PPMI** dataset (47).

External CT benchmarks

Performance on detecting critical neuroradiological findings was evaluated on two public non-contrast head CT cohorts, selected to test generalization on both a large-scale challenge dataset and a smaller, deeply-annotated clinical cohort. The large-scale 2019 **RSNA-ICH** Challenge dataset (48) was used to benchmark multi-label classification of intracranial hemorrhage and its five subtypes (epidural, intraparenchymal, intraventricular, subarachnoid, and subdural). The high-quality, expert-annotated **CQ500** dataset (49) was used for a more extensive evaluation across 14 diagnostic labels, including detailed hemorrhage characterization (subtypes, laterality, chronicity), skull fracture detection, and signs of structural abnormality (e.g., mass effect and midline shift).

Anatomical Probing of NeuroVFM

To test whether NeuroVFM's frozen representations align with neuroanatomy, we paired unsupervised feature analyses with reference neuroanatomical segmentations, which were derived from SynthSeg (12). First, we examined the low-dimensional organization of patch embeddings by running t-SNE on features from representative neuroimages and annotating each point by the majority SynthSeg region (frontal, parietal, temporal, occipital, insula, hippocampus, brainstem, and cerebellum) within its patch. We additionally tested whether NeuroVFM learns an approximate shared anatomical coordinate across subjects, modalities, sequences, and orientations via a patch-matching task. For each query patch from a neuroimage A, we searched over all patches in a different neuroimage B (different subject and acquisition) by L2-normalizing features and identifying the nearest neighbor by cosine similarity. An imaging expert defined a set of canonical neuroanatomical regions (e.g., sella, pineal region, torcula), and we counted a match when both patches lay within the same expert-defined region in their respective scans, without any explicit spatial alignment or supervision. This effectively tests for zero-shot anatomical registration capabilities emergent from the self-supervised objective. Finally, we evaluated whether coarse neuroanatomy emerges without supervision by clustering dense, overlapping patch embeddings computed via sliding-window inference. A k-means model (k = 3) fit on embeddings from the initial window defined canonical clusters that were propagated to all windows and combined into a high-resolution map by voxel-wise majority vote. To identify the brain parenchyma cluster, we computed the IoU between each cluster mask and the SynthSeg brain mask, ultimately selecting the cluster with the highest IoU. Performance was summarized as the mean highest IoU across 30 neuroimages (10 each of axial, sagittal, and coronal natively) from the PPMI dataset, chosen as an external dataset with the full head and neck tissues included.

Vision-Instruction Tuning for Radiology Report Generation

To evaluate NeuroVFM's potential as a visual backbone for multimodal applications, we adapted a LLaVA-1.5-style visual instruction-tuning framework (23). This experiment was designed not to optimize report generation performance, but rather to assess the feasibility of coupling NeuroVFM's learned representations with a large language model (LLM) with minimal architectural modifications.

NeuroVFM-LLaVA architecture

NeuroVFM-LLaVA comprises three components: (1) the frozen NeuroVFM visual encoder, (2) an open-source LLM (Qwen3-14B) (22), and (3) a connector module to bridge them.

Standard LLaVA connectors use a 2-layer MLP to project visual features into the LLM's word embedding space. This approach is insufficient for the high dimensionality of multi-sequence neuroimaging, where a single study may comprise a large and variable number of visual tokens (\geq 20K). To address this, our connector module first employs a perceiver that operates sequence-wise (e.g., on T1, T2, FLAIR independently) (50, 51). The perceiver aggregates the variable-length token sequence from each scan into a fixed-length representation of 64 latents. These fixed-length latents (total latents = 64 × num_sequences) are then concatenated and passed to a 2-layer MLP projector.

Training Dataset and Curation

The training dataset was derived from 444,188 unique neuroimaging studies. To create the text pairs, original radiology reports were summarized using GPT-4.1-mini to extract a concise list of key radiological findings.

Acknowledging that naive training on imbalanced medical datasets can degrade performance, we curated the training set via data resampling. Using the previously extracted diagnostic labels from each report, we performed weighted random sampling with replacement, assigning each study a weight inversely proportional to the prevalence of its rarest associated label. This process, which aims to balance the representation of less common pathologies, resulted in the final training dataset of ~270K unique image-text pairs (444,188 total including duplicates).

Training Strategy

Following the LLaVA methodology, training proceeded in two stages.

- 1. Stage 1 (Connector Pre-training): Only the connector module (perceiver and MLP) weights are updated. The model was trained to map NeuroVFM image features to the corresponding reference key findings, which were formatted as a single, concatenated string.
- 2. Stage 2 (Full Fine-tuning): Both the connector and the LLM weights are updated. In this stage, the model was trained on an instruction-following task. The input prompt was fixed to: "Generate a concise report of the key positive findings for this study." The target output was the same set of findings, but formatted as a structured JSON list ordered by clinical relevance.

Further details on training hyperparameters are provided in Supplementary Data Table 7.

Evaluation of report generation and clinical triage

We evaluated NeuroVFM-LLaVA against two proprietary multimodal frontier models: GPT-5 (*gpt-5-2025-08-07*, "reasoning" medium, "verbosity" low) and Claude Sonnet 4.5 (*claude-sonnet-4-5-20250929*, "thinking" enabled). This evaluation assessed two criteria: (1) the factual accuracy of generated findings and (2) the clinical utility of these findings for a downstream triage task. To support this evaluation, we established Business Associate Agreements (BAAs) with vendors offering commercially available HIPAA-compliant access to frontier models, specifically OpenAI and Anthropic. This enabled the secure exchange of protected health information (PHI) while preserving patient privacy.

Benchmark Model Adaptation (3D-to-2D Conversion)

A primary challenge in benchmarking against proprietary models is that they accept only 2D images and have limitations on total input image tokens. To create a fair comparison with our 3D-native model, we developed a systematic 3D-to-2D conversion pipeline.

- 1. All 3D volumes (preprocessed with the NeuroVFM pipeline) were converted into 224×224 pixel 2D slices by resampling along the axis of acquisition and keeping every other slice.
- 2. Non-diagnostic and derived sequences (e.g., scout images, phase/magnitude maps) were excluded
- 3. Due to API token limits, inputs were constrained to 15 sequences per study for GPT-5 (\sim 360 slices) and 4 for Claude Sonnet 4.5 (\sim 96 slices).
- 4. If a study exceeded this limit, sequences were deterministically prioritized based on clinical relevance (i.e., for MRI: post-contrast T1, DWI/ADC, FLAIR, SWI, T2, non-contrast T1; for CT: at least one brain, blood, and bone window).
- 5. All selected slices were converted to float and normalized between [0,1], and slices with >90% black pixels were dropped.

Evaluation of Generated Reports

All generative models were evaluated on "UM-NeuroImages-Triage", a new, manually-curated test set of 600 studies (300 validation, 300 holdout) derived from our prospective test set. This set was hand-selected by neuroimaging experts to be balanced across three acuity classes ("Unremarkable", "Routine", "Urgent") and two modalities (MRI, CT).

We assessed report quality through automated metrics, BLEU-2 (52), ROUGE-L (53), and METEOR (54), as well as with human evaluation. To ensure effective blinding, all model outputs were standardized to a uniform text format. For NeuroVFM-LLaVA and GPT-5, a neuroimaging expert (T.H.) performed a structured review of each study to quantify (1) capture of key findings, (2) clinically significant hallucinations, and (3) laterality errors. To evaluate preferences, three neuroimaging experts from the United States and Europe (R.J., A.K.M., T.H.) then performed a blinded, randomized pairwise review comparing generated findings from NeuroVFM-LLaVA and GPT-5 against the ground truth clinical report. For each case, model outputs were randomly labeled "Report A" and "Report B". Evaluators selected their preferred report ("Report A", "Report B", or "Both") based on overall clinical utility for triaging. Because Claude Sonnet 4.5 exhibited substantially lower triage accuracy on UM-NeuroImages-Triage, we restricted expert review and preference testing to NeuroVFM-LLaVA and the strongest baseline (GPT-5).

To quantify the clinical utility of the generated findings, we employed an "LLM-as-a-judge" pipeline. In each analysis, we designated a frontier model (GPT-5 or Claude Sonnet 4.5) as a separate "triager LLM", instructed with a strict, pre-defined set of criteria (Supplementary Data Fig. 6). We first confirmed that each triager achieved high accuracy when classifying acuity from the ground-truth radiology report alone. The triager LLM was then prompted to classify each study as "Unremarkable", "Routine", or "Urgent" based solely on the generated text findings from each model (NeuroVFM-LLaVA, GPT-5, and Claude Sonnet 4.5) and the clinical indication. Using GPT-5 vs. Claude Sonnet 4.5 as the triager yielded comparable results, indicating that the protocol is model-agnostic and not biased toward any single frontier model. This procedure converts report generation into a 3-class classification problem and provides a quantitative measure of clinical utility.

Computational hardware and software

All data used to train NeuroVFM were acquired over more than two decades of routine clinical care at Michigan Medicine. Studies were identified in the Michigan Medicine PACS via the SDW. The aggregate size of raw NIfTI volumes is ~150 TB, stored on the ARC DataDen object-storage

service. Post-processing (removal of non-image/corrupt entries and embedded metadata, background removal, and quantization) reduced the footprint by over an order of magnitude to ~9 TB. Preprocessed volumes were written as large NumPy memory-mapped shards (10 shards for the training set; 1 each for the validation and test set) with JSON index manifests to enable zero-copy random access during training.

All experiments were executed on the University of Michigan Advanced Research Computing (ARC) Armis2 cluster using SLURM. Typical jobs used nodes with 8 NVIDIA L40S GPUs (48 GB each), 64 Intel Xeon Platinum 8358 CPU cores, and 503 GB RAM. Vol-JEPA pretraining used PyTorch DistributedDataParallel (DDP), whereas LLM fine-tuning used PyTorch Fully Sharded Data Parallel (FSDP). A full Vol-JEPA pretraining run required <1,000 GPU-hours in aggregate (batch size of 768, ~510K steps), making the approach feasible on university-hosted compute clusters. Training used mixed precision (AMP) with fixed random seeds.

Models were implemented in Python 3.10.14 with PyTorch 2.5.0 (CUDA 12.4). Vol-JEPA pretraining and diagnostic probing used PyTorch Lightning 2.5.0.post0. All data handling and computation occurred on HIPAA-compliant, access-controlled ARC infrastructure. Model weights are available under the CC-BY-NC-SA-4.0 license, enabling the broad dissemination of learned clinical representations without the risk of PHI leakage.

Use of large language models

Large language models were used to assist with code prototyping and manuscript editing. All analyses, text and code were reviewed and verified by the authors, who take full responsibility for the work.

Ethics and inclusion statement

Our research was approved by the University of Michigan Institutional Review Board (HUM00229133). All MRI and CT data were acquired under secondary data usage. The methods were carried out in accordance with the IRB's guidelines, regulations, and policies. All human subjects that met inclusion criteria as stated above were included in the study.

Data availability

Institutional Review Board approval was obtained from University of Michigan for MRI data collection. Restrictions apply to the availability of raw patient MRI and CT imaging data, which were used with institutional permission through IRB approval for the current study and thus are not publicly available. All data sharing between medical centers is regulated through data use agreements with the study authors. A similar data-sharing protocol may be established for interested investigators. Please contact the corresponding author (T.H.) for any requests for data sharing. All requests will be evaluated based on institutional and departmental policies to determine whether the data requested is subject to intellectual property or patient privacy obligations. Data can only be shared for non-commercial academic and investigational purposes.

Code availability

All code was implemented in Python (version 3.10.14) using PyTorch (2.5.0) compiled with CUDA 12.4 as the primary machine learning framework. The following packages were used for data preprocessing, model training and evaluation: pydicom (2.4.4), nibabel (5.3.2), SimpleITK (2.4.0), torchvision (0.20.0), pandas (2.2.3), NumPy (2.1.2), PyTorch Lightning (2.5.0.post0), flash-attn (2.6.3), matplotlib (3.10.7), scipy (1.15.2), and scikit-learn (1.6.1). The following packages were used to load baselines: open-clip

(2.23.0) and transformers (4.56.0). All code and scripts to reproduce the experiments of this paper are available on GitHub at https://github.com/MLNeurosurg/neurovfm under an MIT license.

Acknowledgments

We would like to thank Karen Eddy, Muhammad Bhalli, Gary Laderach, and Brock Palen for providing technical support; David Hanauer for support with the University of Michigan Electronic Medical Record Search Engine (EMERSE); and Anthony Rosenzweig for scientific guidance. This work was supported by the following National Institute of Health (NIH) funding sources: K12NS080223 (T.C.H.), T32GM007863 (A.K., A.R.), and T32GM141746 (A.K.). This work was supported by the Chan Zuckerberg Foundation (CZI) Advancing Imaging Through Collaborative Project grant (T.H.), Cook Family Brain Tumour Research Fund (T.H.), Mark Trauner Brain Research Fund, Zenkel Family Foundation (T.H.), Ian's Friends Foundation (T.H.), UM Precision Health Investigators Awards grant program (T.H.), Translational AI Award from the UM Department of Neurosurgery (T.H.), UM Stanley and Judith Frankel Institute for Heart and Brain Health Innovative Multidisciplinary Research Pilot Award (T.H.) and UM Research Scouts program (T.H.). This research was also supported, in part, through computational resources and services provided by Advanced Research Computing, a division of Information and Technology Services at the University of Michigan.

Author contributions

A.K., A.R., and T.H. contributed to the conceptualization, study design, and analysis of results. A.K., A.R., C.Z., Y.L., S.H., S.B., R.H., C.J., A.C., and T.H. contributed to the experimentation, acquisition, analysis and interpretation of data. A.K., A.R., and T.H. contributed to generating the figures and tables for the manuscript. R.J., A.K.M., and T.H. provided neuroimaging expertise to evaluate generations. All authors were involved in the editing, analysis and review of all data and manuscript versions.

References

- [1] OpenAI. GPT-5: Large language model. https://openai.com/gpt-5, April 2025.
- [2] Oriane Siméoni, Huy V Vo, Maximilian Seitzer, Federico Baldassarre, Maxime Oquab, Cijo Jose, Vasil Khalidov, Marc Szafraniec, Seungeun Yi, Michaël Ramamonjisoa, Francisco Massa, Daniel Haziza, Luca Wehrstedt, Jianyuan Wang, Timothée Darcet, Théo Moutakanni, Leonel Sentana, Claire Roberts, Andrea Vedaldi, Jamie Tolan, John Brandt, Camille Couprie, Julien Mairal, Hervé Jégou, Patrick Labatut, and Piotr Bojanowski. DINOv3. arXiv [cs.CV], August 2025.
- [3] Alexander Ziller, Tamara T Mueller, Simon Stieger, Leonhard F Feiner, Johannes Brandt, Rickmer Braren, Daniel Rueckert, and Georgios Kaissis. Reconciling privacy and accuracy in AI for medical imaging. *Nature Machine Intelligence*, 6(7):764–774, June 2024.
- [4] Yuhao Zhang, Hang Jiang, Yasuhide Miura, Christopher D Manning, and Curtis P Langlotz. Contrastive learning of medical visual representations from paired images and text. In Zachary Lipton, Rajesh Ranganath, Mark Sendak, Michael Sjoding, and Serena Yeung, editors, *Proceedings of the 7th Machine Learning for Healthcare Conference*, volume 182 of *Proceedings of Machine Learning Research*, pages 2–25. PMLR, 2022.
- [5] Alec Radford, Jong Wook Kim, Chris Hallacy, Aditya Ramesh, Gabriel Goh, Sandhini Agarwal, Girish Sastry, Amanda Askell, Pamela Mishkin, Jack Clark, Gretchen Krueger, and Ilya Sutskever. Learning transferable visual models from natural language supervision. In Marina Meila and Tong Zhang, editors, *Proceedings of the 38th International Conference on Machine Learning*, volume 139 of *Proceedings of Machine Learning Research*, pages 8748–8763. PMLR, 2021.

- [6] Yann LeCun. A path towards autonomous machine intelligence (version 0.9.2, 2022-06-27). OpenReview preprint, ID: BZ5a1r-kVsf, June 2022.
- [7] Yiwei Lyu, Samir Harake, Asadur Chowdury, Soumyanil Banerjee, Rachel Gologorsky, Shixuan Liu, Anna-Katharina Meissner, Akshay Rao, Akhil Kondepudi, Cheng Jiang, Xinhai Hou, Rushikesh Joshi, Volker Neuschmelting, Ashok Srinivasan, Dawn Kleindorfer, Brian Athey, Vikas Gulani, Aditya Pandey, Honglak Lee, and Todd Hollon. Learning neuroimaging models from health system-scale data. *Res. Sq.*, February 2025.
- [8] Mahmoud Assran, Quentin Duval, Ishan Misra, Piotr Bojanowski, Pascal Vincent, Michael Rabbat, Yann LeCun, and Nicolas Ballas. Self-supervised learning from images with a joint-embedding predictive architecture. *arXiv* [cs.CV], January 2023.
- [9] Mido Assran, Adrien Bardes, David Fan, Quentin Garrido, Russell Howes, Mojtaba, Komeili, Matthew Muckley, Ammar Rizvi, Claire Roberts, Koustuv Sinha, Artem Zholus, Sergio Arnaud, Abha Gejji, Ada Martin, Francois Robert Hogan, Daniel Dugas, Piotr Bojanowski, Vasil Khalidov, Patrick Labatut, Francisco Massa, Marc Szafraniec, Kapil Krishnakumar, Yong Li, Xiaodong Ma, Sarath Chandar, Franziska Meier, Yann LeCun, Michael Rabbat, and Nicolas Ballas. V-JEPA 2: Self-supervised video models enable understanding, prediction and planning. arXiv [cs.AI], June 2025.
- [10] Adrien Bardes, Quentin Garrido, Jean Ponce, Xinlei Chen, Michael Rabbat, Yann LeCun, Mahmoud Assran, and Nicolas Ballas. Revisiting feature prediction for learning visual representations from video. *arXiv* [cs.CV], February 2024.
- [11] Alexey Dosovitskiy, Lucas Beyer, Alexander Kolesnikov, Dirk Weissenborn, Xiaohua Zhai, Thomas Unterthiner, Mostafa Dehghani, Matthias Minderer, Georg Heigold, Sylvain Gelly, Jakob Uszkoreit, and Neil Houlsby. An image is worth 16x16 words: Transformers for image recognition at scale. September 2020.
- [12] Benjamin Billot, Douglas N Greve, Oula Puonti, Axel Thielscher, Koen Van Leemput, Bruce Fischl, Adrian V Dalca, Juan Eugenio Iglesias, and ADNI. SynthSeg: Segmentation of brain MRI scans of any contrast and resolution without retraining. *Med. Image Anal.*, 86(102789):102789, May 2023.
- [13] Chenhui Zhao, Yiwei Lyu, Asadur Chowdury, Edward Harake, Akhil Kondepudi, Akshay Rao, Xinhai Hou, Honglak Lee, and Todd Hollon. Towards scalable language-image pre-training for 3D medical imaging. *arXiv* [cs.CV], May 2025.
- [14] J H Pexman, P A Barber, M D Hill, R J Sevick, A M Demchuk, M E Hudon, W Y Hu, and A M Buchan. Use of the alberta stroke program early CT score (ASPECTS) for assessing CT scans in patients with acute stroke. *AJNR Am. J. Neuroradiol.*, 22(8):1534–1542, September 2001.
- [15] Sohil H Patel, Laila M Poisson, Daniel J Brat, Yueren Zhou, Lee Cooper, Matija Snuderl, Cheddhi Thomas, Ana M Franceschi, Brent Griffith, Adam E Flanders, John G Golfinos, Andrew S Chi, and Rajan Jain. T2-FLAIR mismatch, an imaging biomarker for IDH and 1p/19q status in lower-grade gliomas: A TCGA/TCIA project. *Clin. Cancer Res.*, 23(20):6078–6085, October 2017.
- [16] Jared Kaplan, Sam McCandlish, Tom Henighan, Tom B Brown, Benjamin Chess, Rewon Child, Scott Gray, Alec Radford, Jeffrey Wu, and Dario Amodei. Scaling laws for neural language models. *arXiv* [cs.LG], January 2020.
- [17] Maximilian Ilse, Jakub Tomczak, and Max Welling. Attention-based deep multiple instance learning. In Jennifer Dy and Andreas Krause, editors, *Proceedings of the 35th International Conference*

- on Machine Learning, volume 80 of Proceedings of Machine Learning Research, pages 2127–2136. PMLR, 2018.
- [18] Vincent Planche, José V Manjon, Boris Mansencal, Enrique Lanuza, Thomas Tourdias, Gwenaëlle Catheline, and Pierrick Coupé. Structural progression of alzheimer's disease over decades: the MRI staging scheme. *Brain Commun.*, 4(3):fcac109, April 2022.
- [19] Jason Wei, Yi Tay, Rishi Bommasani, Colin Raffel, Barret Zoph, Sebastian Borgeaud, Dani Yogatama, Maarten Bosma, Denny Zhou, Donald Metzler, Ed H Chi, Tatsunori Hashimoto, Oriol Vinyals, Percy Liang, Jeff Dean, and William Fedus. Emergent abilities of large language models. arXiv [cs.CL], June 2022.
- [20] Joseph J Titano, Marcus Badgeley, Javin Schefflein, Margaret Pain, Andres Su, Michael Cai, Nathaniel Swinburne, John Zech, Jun Kim, Joshua Bederson, J Mocco, Burton Drayer, Joseph Lehar, Samuel Cho, Anthony Costa, and Eric K Oermann. Automated deep-neural-network surveillance of cranial images for acute neurologic events. *Nat. Med.*, 24(9):1337–1341, September 2018.
- [21] David A Wood, Sina Kafiabadi, Ayisha Al Busaidi, Emily Guilhem, Antanas Montvila, Jeremy Lynch, Matthew Townend, Siddharth Agarwal, Asif Mazumder, Gareth J Barker, Sebastien Ourselin, James H Cole, and Thomas C Booth. Deep learning models for triaging hospital head MRI examinations. *Med. Image Anal.*, 78(102391):102391, May 2022.
- [22] An Yang, Anfeng Li, Baosong Yang, Beichen Zhang, Binyuan Hui, Bo Zheng, Bowen Yu, Chang Gao, Chengen Huang, Chenxu Lv, Chujie Zheng, Dayiheng Liu, Fan Zhou, Fei Huang, Feng Hu, Hao Ge, Haoran Wei, Huan Lin, Jialong Tang, Jian Yang, Jianhong Tu, Jianwei Zhang, Jianxin Yang, Jiaxi Yang, Jing Zhou, Jingren Zhou, Junyang Lin, Kai Dang, Keqin Bao, Kexin Yang, Le Yu, Lianghao Deng, Mei Li, Mingfeng Xue, Mingze Li, Pei Zhang, Peng Wang, Qin Zhu, Rui Men, Ruize Gao, Shixuan Liu, Shuang Luo, Tianhao Li, Tianyi Tang, Wenbiao Yin, Xingzhang Ren, Xinyu Wang, Xinyu Zhang, Xuancheng Ren, Yang Fan, Yang Su, Yichang Zhang, Yinger Zhang, Yu Wan, Yuqiong Liu, Zekun Wang, Zeyu Cui, Zhenru Zhang, Zhipeng Zhou, and Zihan Qiu. Qwen3 technical report. arXiv [cs.CL], May 2025.
- [23] Haotian Liu, Chunyuan Li, Yuheng Li, and Yong Jae Lee. Improved baselines with visual instruction tuning, 2023.
- [24] Balestriero Randall and Lecun Yann. LeJEPA: Provable and scalable self-supervised learning without the heuristics. *arXiv* [cs.LG], November 2025.
- [25] Lavender Yao Jiang, Xujin Chris Liu, Nima Pour Nejatian, Mustafa Nasir-Moin, Duo Wang, Anas Abidin, Kevin Eaton, Howard Antony Riina, Ilya Laufer, Paawan Punjabi, Madeline Miceli, Nora C Kim, Cordelia Orillac, Zane Schnurman, Christopher Livia, Hannah Weiss, David Kurland, Sean Neifert, Yosef Dastagirzada, Douglas Kondziolka, Alexander T M Cheung, Grace Yang, Ming Cao, Mona Flores, Anthony B Costa, Yindalon Aphinyanaphongs, Kyunghyun Cho, and Eric Karl Oermann. Health system-scale language models are all-purpose prediction engines. *Nature*, 619(7969):357–362, July 2023.
- [26] Artem Shmatko, Alexander Wolfgang Jung, Kumar Gaurav, Søren Brunak, Laust Hvas Mortensen, Ewan Birney, Tom Fitzgerald, and Moritz Gerstung. Learning the natural history of human disease with generative transformers. *Nature*, 647(8088):248–256, November 2025.
- [27] David Ha and Jürgen Schmidhuber. World models. arXiv [cs.LG], March 2018.

- [28] Danijar Hafner, Jurgis Pasukonis, Jimmy Ba, and Timothy Lillicrap. Mastering diverse control tasks through world models. *Nature*, 640(8059):647–653, April 2025.
- [29] Quentin Garrido, Mahmoud Assran, Nicolas Ballas, Adrien Bardes, Laurent Najman, and Yann LeCun. Learning and leveraging world models in visual representation learning. arXiv [cs.CV], March 2024.
- [30] OpenAI, Aaron Jaech, Adam Kalai, Adam Lerer, Adam Richardson, Ahmed El-Kishky, Aiden Low, Alec Helyar, Aleksander Madry, Alex Beutel, Alex Carney, Alex Iftimie, Alex Karpenko, Alex Tachard Passos, Alexander Neitz, Alexander Prokofiev, Alexander Wei, Allison Tam, Ally Bennett, Ananya Kumar, Andre Saraiva, Andrea Vallone, Andrew Duberstein, Andrew Kondrich, Andrey Mishchenko, Andy Applebaum, Angela Jiang, Ashvin Nair, Barret Zoph, Behrooz Ghorbani, Ben Rossen, Benjamin Sokolowsky, Boaz Barak, Bob McGrew, Borys Minaiev, Botao Hao, Bowen Baker, Brandon Houghton, Brandon McKinzie, Brydon Eastman, Camillo Lugaresi, Cary Bassin, Cary Hudson, Chak Ming Li, Charles de Bourcy, Chelsea Voss, Chen Shen, Chong Zhang, Chris Koch, Chris Orsinger, Christopher Hesse, Claudia Fischer, Clive Chan, Dan Roberts, Daniel Kappler, Daniel Levy, Daniel Selsam, David Dohan, David Farhi, David Mely, David Robinson, Dimitris Tsipras, Doug Li, Dragos Oprica, Eben Freeman, Eddie Zhang, Edmund Wong, Elizabeth Proehl, Enoch Cheung, Eric Mitchell, Eric Wallace, Erik Ritter, Evan Mays, Fan Wang, Felipe Petroski Such, Filippo Raso, Florencia Leoni, Foivos Tsimpourlas, Francis Song, Fred von Lohmann, Freddie Sulit, Geoff Salmon, Giambattista Parascandolo, Gildas Chabot, Grace Zhao, Greg Brockman, Guillaume Leclerc, Hadi Salman, Haiming Bao, Hao Sheng, Hart Andrin, Hessam Bagherinezhad, Hongyu Ren, Hunter Lightman, Hyung Won Chung, Ian Kivlichan, Ian O'Connell, Ian Osband, Ignasi Clavera Gilaberte, Ilge Akkaya, Ilya Kostrikov, Ilya Sutskever, Irina Kofman, Jakub Pachocki, James Lennon, Jason Wei, Jean Harb, Jerry Twore, Jiacheng Feng, Jiahui Yu, Jiayi Weng, Jie Tang, Jieqi Yu, Joaquin Quiñonero Candela, Joe Palermo, Joel Parish, Johannes Heidecke, John Hallman, John Rizzo, Jonathan Gordon, Jonathan Uesato, Jonathan Ward, Joost Huizinga, Julie Wang, Kai Chen, Kai Xiao, Karan Singhal, Karina Nguyen, Karl Cobbe, Katy Shi, Kayla Wood, Kendra Rimbach, Keren Gu-Lemberg, Kevin Liu, Kevin Lu, Kevin Stone, Kevin Yu, Lama Ahmad, Lauren Yang, Leo Liu, Leon Maksin, Leyton Ho, Liam Fedus, Lilian Weng, Linden Li, Lindsay McCallum, Lindsey Held, Lorenz Kuhn, Lukas Kondraciuk, Lukasz Kaiser, Luke Metz, Madelaine Boyd, Maja Trebacz, Manas Joglekar, Mark Chen, Marko Tintor, Mason Meyer, Matt Jones, Matt Kaufer, Max Schwarzer, Meghan Shah, Mehmet Yatbaz, Melody Y Guan, Mengyuan Xu, Mengyuan Yan, Mia Glaese, Mianna Chen, Michael Lampe, Michael Malek, Michele Wang, Michelle Fradin, Mike McClay, Mikhail Pavlov, Miles Wang, Mingxuan Wang, Mira Murati, Mo Bavarian, Mostafa Rohaninejad, Nat McAleese, Neil Chowdhury, Neil Chowdhury, Nick Ryder, Nikolas Tezak, Noam Brown, Ofir Nachum, Oleg Boiko, Oleg Murk, Olivia Watkins, Patrick Chao, Paul Ashbourne, Pavel Izmailov, Peter Zhokhov, Rachel Dias, Rahul Arora, Randall Lin, Rapha Gontijo Lopes, Raz Gaon, Reah Miyara, Reimar Leike, Renny Hwang, Rhythm Garg, Robin Brown, Roshan James, Rui Shu, Ryan Cheu, Ryan Greene, Saachi Jain, Sam Altman, Sam Toizer, Sam Toyer, Samuel Miserendino, Sandhini Agarwal, Santiago Hernandez, Sasha Baker, Scott McKinney, Scottie Yan, Shengjia Zhao, Shengli Hu, Shibani Santurkar, Shraman Ray Chaudhuri, Shuyuan Zhang, Siyuan Fu, Spencer Papay, Steph Lin, Suchir Balaji, Suvansh Sanjeev, Szymon Sidor, Tal Broda, Aidan Clark, Tao Wang, Taylor Gordon, Ted Sanders, Tejal Patwardhan, Thibault Sottiaux, Thomas Degry, Thomas Dimson, Tianhao Zheng, Timur Garipov, Tom Stasi, Trapit Bansal, Trevor Creech, Troy Peterson, Tyna Eloundou, Valerie Qi, Vineet Kosaraju, Vinnie Monaco, Vitchyr Pong, Vlad Fomenko, Weiyi Zheng, Wenda Zhou, Wes McCabe, Wojciech Zaremba, Yann Dubois, Yinghai Lu, Yining Chen, Young Cha, Yu Bai, Yuchen He, Yuchen Zhang, Yunyun Wang, Zheng Shao, and Zhuohan Li. OpenAI o1 system card. arXiv [cs.AI], December 2024.

- [31] Daya Guo, Dejian Yang, Haowei Zhang, Junxiao Song, Peiyi Wang, Qihao Zhu, Runxin Xu, Ruoyu Zhang, Shirong Ma, Xiao Bi, Xiaokang Zhang, Xingkai Yu, Yu Wu, Z F Wu, Zhibin Gou, Zhihong Shao, Zhuoshu Li, Ziyi Gao, Aixin Liu, Bing Xue, Bingxuan Wang, Bochao Wu, Bei Feng, Chengda Lu, Chenggang Zhao, Chengqi Deng, Chong Ruan, Damai Dai, Deli Chen, Dongjie Ji, Erhang Li, Fangyun Lin, Fucong Dai, Fuli Luo, Guangbo Hao, Guanting Chen, Guowei Li, H Zhang, Hanwei Xu, Honghui Ding, Huazuo Gao, Hui Qu, Hui Li, Jianzhong Guo, Jiashi Li, Jingchang Chen, Jingyang Yuan, Jinhao Tu, Junjie Qiu, Junlong Li, J L Cai, Jiaqi Ni, Jian Liang, Jin Chen, Kai Dong, Kai Hu, Kaichao You, Kaige Gao, Kang Guan, Kexin Huang, Kuai Yu, Lean Wang, Lecong Zhang, Liang Zhao, Litong Wang, Liyue Zhang, Lei Xu, Leyi Xia, Mingchuan Zhang, Minghua Zhang, Minghui Tang, Mingxu Zhou, Meng Li, Miaojun Wang, Mingming Li, Ning Tian, Panpan Huang, Peng Zhang, Qiancheng Wang, Qinyu Chen, Qiushi Du, Ruiqi Ge, Ruisong Zhang, Ruizhe Pan, Runji Wang, R J Chen, R L Jin, Ruyi Chen, Shanghao Lu, Shangyan Zhou, Shanhuang Chen, Shengfeng Ye, Shiyu Wang, Shuiping Yu, Shunfeng Zhou, Shuting Pan, S S Li, Shuang Zhou, Shaoqing Wu, Tao Yun, Tian Pei, Tianyu Sun, T Wang, Wangding Zeng, Wen Liu, Wenfeng Liang, Wenjun Gao, Wenqin Yu, Wentao Zhang, W L Xiao, Wei An, Xiaodong Liu, Xiaohan Wang, Xiaokang Chen, Xiaotao Nie, Xin Cheng, Xin Liu, Xin Xie, Xingchao Liu, Xinyu Yang, Xinyuan Li, Xuecheng Su, Xuheng Lin, X Q Li, Xiangyue Jin, Xiaojin Shen, Xiaosha Chen, Xiaowen Sun, Xiaoxiang Wang, Xinnan Song, Xinyi Zhou, Xianzu Wang, Xinxia Shan, Y K Li, Y Q Wang, Y X Wei, Yang Zhang, Yanhong Xu, Yao Li, Yao Zhao, Yaofeng Sun, Yaohui Wang, Yi Yu, Yichao Zhang, Yifan Shi, Yiliang Xiong, Ying He, Yishi Piao, Yisong Wang, Yixuan Tan, Yiyang Ma, Yiyuan Liu, Yongqiang Guo, Yuan Ou, Yuduan Wang, Yue Gong, Yuheng Zou, Yujia He, Yunfan Xiong, Yuxiang Luo, Yuxiang You, Yuxuan Liu, Yuyang Zhou, Y X Zhu, Yanping Huang, Yaohui Li, Yi Zheng, Yuchen Zhu, Yunxian Ma, Ying Tang, Yukun Zha, Yuting Yan, Z Z Ren, Zehui Ren, Zhangli Sha, Zhe Fu, Zhean Xu, Zhenda Xie, Zhengyan Zhang, Zhewen Hao, Zhicheng Ma, Zhigang Yan, Zhiyu Wu, Zihui Gu, Zijia Zhu, Zijun Liu, Zilin Li, Ziwei Xie, Ziyang Song, Zizheng Pan, Zhen Huang, Zhipeng Xu, Zhongyu Zhang, and Zhen Zhang. DeepSeek-R1 incentivizes reasoning in LLMs through reinforcement learning. Nature, 645(8081):633-638, September 2025.
- [32] Pan Lu, Bowen Chen, Sheng Liu, Rahul Thapa, Joseph Boen, and James Zou. OctoTools: An agentic framework with extensible tools for complex reasoning. *arXiv* [cs.LG], February 2025.
- [33] Michael Moor, Oishi Banerjee, Zahra Shakeri Hossein Abad, Harlan M Krumholz, Jure Leskovec, Eric J Topol, and Pranav Rajpurkar. Foundation models for generalist medical artificial intelligence. *Nature*, 616(7956):259–265, April 2023.
- [34] Lisa C Adams, Daniel Truhn, Felix Busch, Avan Kader, Stefan M Niehues, Marcus R Makowski, and Keno K Bressem. Leveraging GPT-4 for post hoc transformation of free-text radiology reports into structured reporting: A multilingual feasibility study. *Radiology*, 307(4):e230725, May 2023.
- [35] Aichi Chien, Hubert Tang, Bhavita Jagessar, Kai-Wei Chang, Nanyun Peng, Kambiz Nael, and Noriko Salamon. AI-assisted summarization of radiologic reports: Evaluating GPT3davinci, BARTcnn, LongT5booksum, LEDbooksum, LEDlegal, and LEDclinical. *AJNR Am. J. Neuroradiol.*, 45(2):244–248, February 2024.
- [36] Mercy Ranjit, Gopinath Ganapathy, Ranjit Manuel, and Tanuja Ganu. Retrieval augmented chest X-ray report generation using OpenAI GPT models. In *Machine Learning for Healthcare Conference*, pages 650–666. PMLR, December 2023.
- [37] Tri Dao. FlashAttention-2: Faster attention with better parallelism and work partitioning. *arXiv* [cs.LG], July 2023.

- [38] Richard J Chen, Tong Ding, Ming Y Lu, Drew F K Williamson, Guillaume Jaume, Andrew H Song, Bowen Chen, Andrew Zhang, Daniel Shao, Muhammad Shaban, Mane Williams, Lukas Oldenburg, Luca L Weishaupt, Judy J Wang, Anurag Vaidya, Long Phi Le, Georg Gerber, Sharifa Sahai, Walt Williams, and Faisal Mahmood. Towards a general-purpose foundation model for computational pathology. *Nat. Med.*, 30(3):850–862, March 2024.
- [39] Sheng Zhang, Yanbo Xu, Naoto Usuyama, Jaspreet Bagga, Robert Tinn, Sam Preston, Rajesh Rao, Mu Wei, Naveen Valluri, Cliff Wong, Matthew Lungren, Tristan Naumann, and Hoifung Poon. Large-scale domain-specific pretraining for biomedical vision-language processing, 2023. URL https://arxiv.org/abs/2303.00915.
- [40] Zhan Tong, Yibing Song, Jue Wang, and Limin Wang. VideoMAE: masked autoencoders are data-efficient learners for self-supervised video pre-training. In *Proceedings of the 36th International* Conference on Neural Information Processing Systems, number Article 732 in NIPS '22, pages 10078– 10093, Red Hook, NY, USA, November 2022. Curran Associates Inc.
- [41] Maxime Oquab, Timothée Darcet, Théo Moutakanni, Huy Vo, Marc Szafraniec, Vasil Khalidov, Pierre Fernandez, Daniel Haziza, Francisco Massa, Alaaeldin El-Nouby, Mahmoud Assran, Nicolas Ballas, Wojciech Galuba, Russell Howes, Po-Yao Huang, Shang-Wen Li, Ishan Misra, Michael Rabbat, Vasu Sharma, Gabriel Synnaeve, Hu Xu, Hervé Jegou, Julien Mairal, Patrick Labatut, Armand Joulin, and Piotr Bojanowski. DINOv2: Learning robust visual features without supervision. *arXiv* [cs.CV], April 2023.
- [42] Benoit Dufumier, Antoine Grigis, Julie Victor, Corentin Ambroise, Vincent Frouin, and Edouard Duchesnay. OpenBHB: A large-scale multi-site brain MRI data-set for age prediction and debiasing. *Neuroimage*, 263(119637):119637, November 2022.
- [43] Ronald Carl Petersen, Paul S Aisen, Laurel A Beckett, Michael C Donohue, Anthony Collins Gamst, Danielle J Harvey, CR Jack Jr, William J Jagust, Leslie M Shaw, Arthur W Toga, et al. Alzheimer's disease neuroimaging initiative (adni) clinical characterization. *Neurology*, 74(3): 201–209, 2010.
- [44] Daniel S Marcus, Anthony F Fotenos, John G Csernansky, John C Morris, and Randy L Buckner. Open access series of imaging studies: longitudinal MRI data in nondemented and demented older adults. *J. Cogn. Neurosci.*, 22(12):2677–2684, December 2010.
- [45] Christopher Fowler, Stephanie R Rainey-Smith, Sabine Bird, Julia Bomke, Pierrick Bourgeat, Belinda M Brown, Samantha C Burnham, Ashley I Bush, Carolyn Chadunow, Steven Collins, James Doecke, Vincent Doré, Kathryn A Ellis, Lis Evered, Amir Fazlollahi, Jurgen Fripp, Samantha L Gardener, Simon Gibson, Robert Grenfell, Elise Harrison, Richard Head, Liang Jin, Adrian Kamer, Fiona Lamb, Nicola T Lautenschlager, Simon M Laws, Qiao-Xin Li, Lucy Lim, Yen Ying Lim, Andrea Louey, S Lance Macaulay, Lucy Mackintosh, Ralph N Martins, Paul Maruff, Colin L Masters, Simon McBride, Lidija Milicic, Madeline Peretti, Kelly Pertile, Tenielle Porter, Morgan Radler, Alan Rembach, Joanne Robertson, Mark Rodrigues, Christopher C Rowe, Rebecca Rumble, Olivier Salvado, Greg Savage, Brendan Silbert, Magdalene Soh, Hamid R Sohrabi, Kevin Taddei, Tania Taddei, Christine Thai, Brett Trounson, Regan Tyrrell, Michael Vacher, Shiji Varghese, Victor L Villemagne, Michael Weinborn, Michael Woodward, Ying Xia, David Ames, and the AIBL investigators. Fifteen years of the australian imaging, biomarkers and lifestyle (AIBL) study: Progress and observations from 2,359 older adults spanning the spectrum from cognitive normality to alzheimer's disease. *J. Alzheimers Dis. Rep.*, 5(1):443–468, June 2021.
- [46] A Di Martino, C-G Yan, Q Li, E Denio, F X Castellanos, K Alaerts, J S Anderson, M Assaf, S Y Bookheimer, M Dapretto, B Deen, S Delmonte, I Dinstein, B Ertl-Wagner, D A Fair, L Gallagher,

- D P Kennedy, C L Keown, C Keysers, J E Lainhart, C Lord, B Luna, V Menon, N J Minshew, C S Monk, S Mueller, R-A Müller, M B Nebel, J T Nigg, K O'Hearn, K A Pelphrey, S J Peltier, J D Rudie, S Sunaert, M Thioux, J M Tyszka, L Q Uddin, J S Verhoeven, N Wenderoth, J L Wiggins, S H Mostofsky, and M P Milham. The autism brain imaging data exchange: towards a large-scale evaluation of the intrinsic brain architecture in autism. *Mol. Psychiatry*, 19(6):659–667, June 2014.
- [47] Kenneth Marek, Sohini Chowdhury, Andrew Siderowf, Shirley Lasch, Christopher S Coffey, Chelsea Caspell-Garcia, Tanya Simuni, Danna Jennings, Caroline M Tanner, John Q Trojanowski, Leslie M Shaw, John Seibyl, Norbert Schuff, Andrew Singleton, Karl Kieburtz, Arthur W Toga, Brit Mollenhauer, Doug Galasko, Lana M Chahine, Daniel Weintraub, Tatiana Foroud, Duygu Tosun-Turgut, Kathleen Poston, Vanessa Arnedo, Mark Frasier, Todd Sherer, and Parkinson's Progression Markers Initiative. The parkinson's progression markers initiative (PPMI) establishing a PD biomarker cohort. *Ann. Clin. Transl. Neurol.*, 5(12):1460–1477, December 2018.
- [48] Adam E Flanders, Luciano M Prevedello, George Shih, Safwan S Halabi, Jayashree Kalpathy-Cramer, Robyn Ball, John T Mongan, Anouk Stein, Felipe C Kitamura, Matthew P Lungren, Gagandeep Choudhary, Lesley Cala, Luiz Coelho, Monique Mogensen, Fanny Morón, Elka Miller, Ichiro Ikuta, Vahe Zohrabian, Olivia McDonnell, Christie Lincoln, Lubdha Shah, David Joyner, Amit Agarwal, Ryan K Lee, Jaya Nath, and RSNA-ASNR 2019 Brain Hemorrhage CT Annotators. Construction of a machine learning dataset through collaboration: The RSNA 2019 brain CT hemorrhage challenge. *Radiol. Artif. Intell.*, 2(3):e190211, May 2020.
- [49] Sasank Chilamkurthy, Rohit Ghosh, Swetha Tanamala, Mustafa Biviji, Norbert G Campeau, Vasantha Kumar Venugopal, Vidur Mahajan, Pooja Rao, and Prashant Warier. Deep learning algorithms for detection of critical findings in head CT scans: a retrospective study. *Lancet*, 392 (10162):2388–2396, December 2018.
- [50] Jean-Baptiste Alayrac, Jeff Donahue, Pauline Luc, Antoine Miech, Iain Barr, Yana Hasson, Karel Lenc, Arthur Mensch, Katie Millican, Malcolm Reynolds, Roman Ring, Eliza Rutherford, Serkan Cabi, Tengda Han, Zhitao Gong, Sina Samangooei, Marianne Monteiro, Jacob Menick, Sebastian Borgeaud, Andrew Brock, Aida Nematzadeh, Sahand Sharifzadeh, Mikolaj Binkowski, Ricardo Barreira, Oriol Vinyals, Andrew Zisserman, and Karen Simonyan. Flamingo: a visual language model for few-shot learning. arXiv [cs.CV], April 2022.
- [51] Andrew Jaegle, Felix Gimeno, Andrew Brock, Andrew Zisserman, Oriol Vinyals, and Joao Carreira. Perceiver: General perception with iterative attention. *arXiv* [cs.CV], March 2021.
- [52] Kishore Papineni, Salim Roukos, Todd Ward, and Wei-Jing Zhu. BLEU: a method for automatic evaluation of machine translation. In *Proceedings of the 40th Annual Meeting on Association for Computational Linguistics ACL '02*, Morristown, NJ, USA, 2001. Association for Computational Linguistics.
- [53] Chin-Yew Lin and Franz Josef Och. Automatic evaluation of machine translation quality using longest common subsequence and skip-bigram statistics. In *Proceedings of the 42nd Annual Meeting on Association for Computational Linguistics ACL '04*, pages 605–612, Morristown, NJ, USA, 2004. Association for Computational Linguistics.
- [54] Satanjeev Banerjee and Alon Lavie. METEOR: An automatic metric for MT evaluation with improved correlation with human judgments. In *Proceedings of the ACL Workshop on Intrinsic and Extrinsic Evaluation Measures for Machine Translation and/or Summarization*, pages 65–72, 2005.
- [55] Conor S Gillespie, John Gerrard Hanrahan, Roxana Mahdiyar, Keng Siang Lee, Mohammad Ashraf, Ali M Alam, Justyna O Ekert, Orla Mantle, Simon C Williams, Jonathan P Funnell,

- Nihal Gurusinghe, Raghu Vindlacheruvu, Peter C Whitfield, Rikin A Trivedi, Adel Helmy, and Peter J Hutchinson. Diagnosis of subarachnoid haemorrhage: Systematic evaluation of CT head diagnostic accuracy and comparison with the 2022 NICE guidelines. *Brain Spine*, 5(104200): 104200, February 2025.
- [56] Romane Gauriau, Bernardo C Bizzo, Donnella S Comeau, James M Hillis, Christopher P Bridge, John K Chin, Jayashri Pawar, Ali Pourvaziri, Ivana Sesic, Elshaimaa Sharaf, Jinjin Cao, Flavia T C Noro, Walter F Wiggins, M Travis Caton, Felipe Kitamura, Keith J Dreyer, John F Kalafut, Katherine P Andriole, Stuart R Pomerantz, Ramon G Gonzalez, and Michael H Lev. Head CT deep learning model is highly accurate for early infarct estimation. *Sci. Rep.*, 13(1):189, January 2023.
- [57] Antonios Thanellas, Heikki Peura, Mikko Lavinto, Tomi Ruokola, Moira Vieli, Victor E Staartjes, Sebastian Winklhofer, Carlo Serra, Luca Regli, and Miikka Korja. Development and external validation of a deep learning algorithm to identify and localize subarachnoid hemorrhage on CT scans. *Neurology*, 100(12):e1257–e1266, March 2023.
- [58] X Z Chen, X M Yin, L Ai, Q Chen, S W Li, and J P Dai. Differentiation between brain glioblastoma multiforme and solitary metastasis: qualitative and quantitative analysis based on routine MR imaging. *AJNR Am. J. Neuroradiol.*, 33(10):1907–1912, November 2012.
- [59] Gianfranco Di Salle, Lorenzo Tumminello, Maria Elena Laino, Sherif Shalaby, Gayane Aghakhanyan, Salvatore Claudio Fanni, Maria Febi, Jorge Eduardo Shortrede, Mario Miccoli, Lorenzo Faggioni, Mirco Cosottini, and Emanuele Neri. Accuracy of radiomics in predicting IDH mutation status in diffuse gliomas: A bivariate meta-analysis. *Radiol. Artif. Intell.*, 6(1):e220257, January 2024.
- [60] Xueming Xia, Wenjun Wu, Qiaoyue Tan, and Qiheng Gou. Interpretable machine learning models for differentiating glioblastoma from solitary brain metastasis using radiomics. *Acad. Radiol.*, 32 (9):5388–5400, September 2025.
- [61] Nidhal Jegham, Marwan Abdelatti, Lassad Elmoubarki, and Abdeltawab Hendawi. How hungry is AI? benchmarking energy, water, and carbon footprint of LLM inference. *arXiv* [cs.CY], September 2025.

A. Extended Data Figures

- 1. Extended NeuroVFM workflow
- 2. Overview of UM-NeuroImages
- 3. Learning with Vol-JEPA
- 4. Extended CT diagnostic results
- 5. Extended MRI diagnostic results
- 6. Subgroup and health system analysis
- 7. Open benchmark performance
- 8. Neuroimage scene understanding and grounded diagnoses
- 9. Generative evaluation
- 10. Generated triage reports

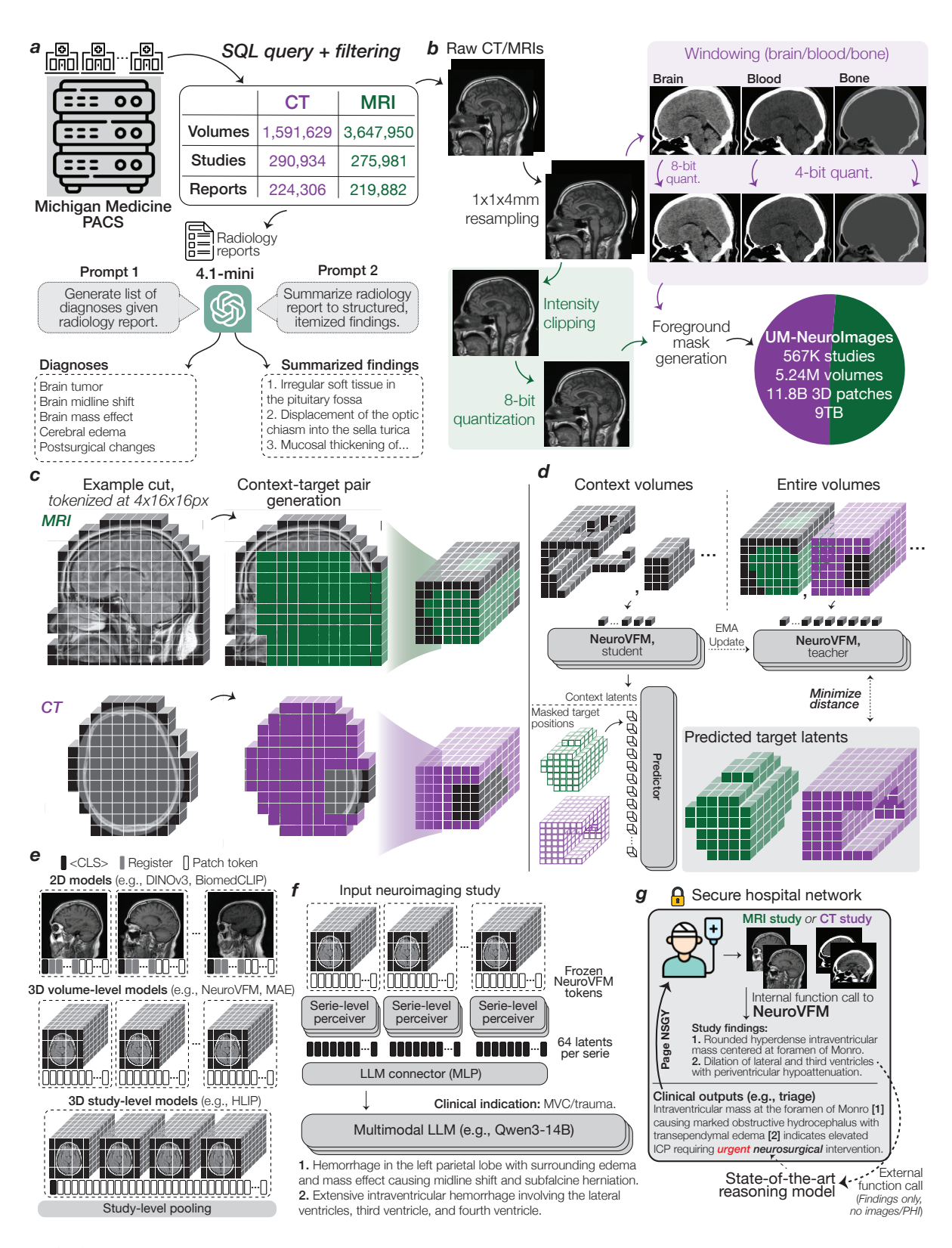
B. Supplementary Data

B.1. Supplementary Data Figures

- 1. SQL query for UM-NeuroImages curation
- 2. MRI diagnoses extraction prompt
- 3. CT diagnoses extraction prompt
- 4. Prompts for structured findings extraction
- 5. Frontier model prompt for study findings
- 6. Triage prompt given findings and indication

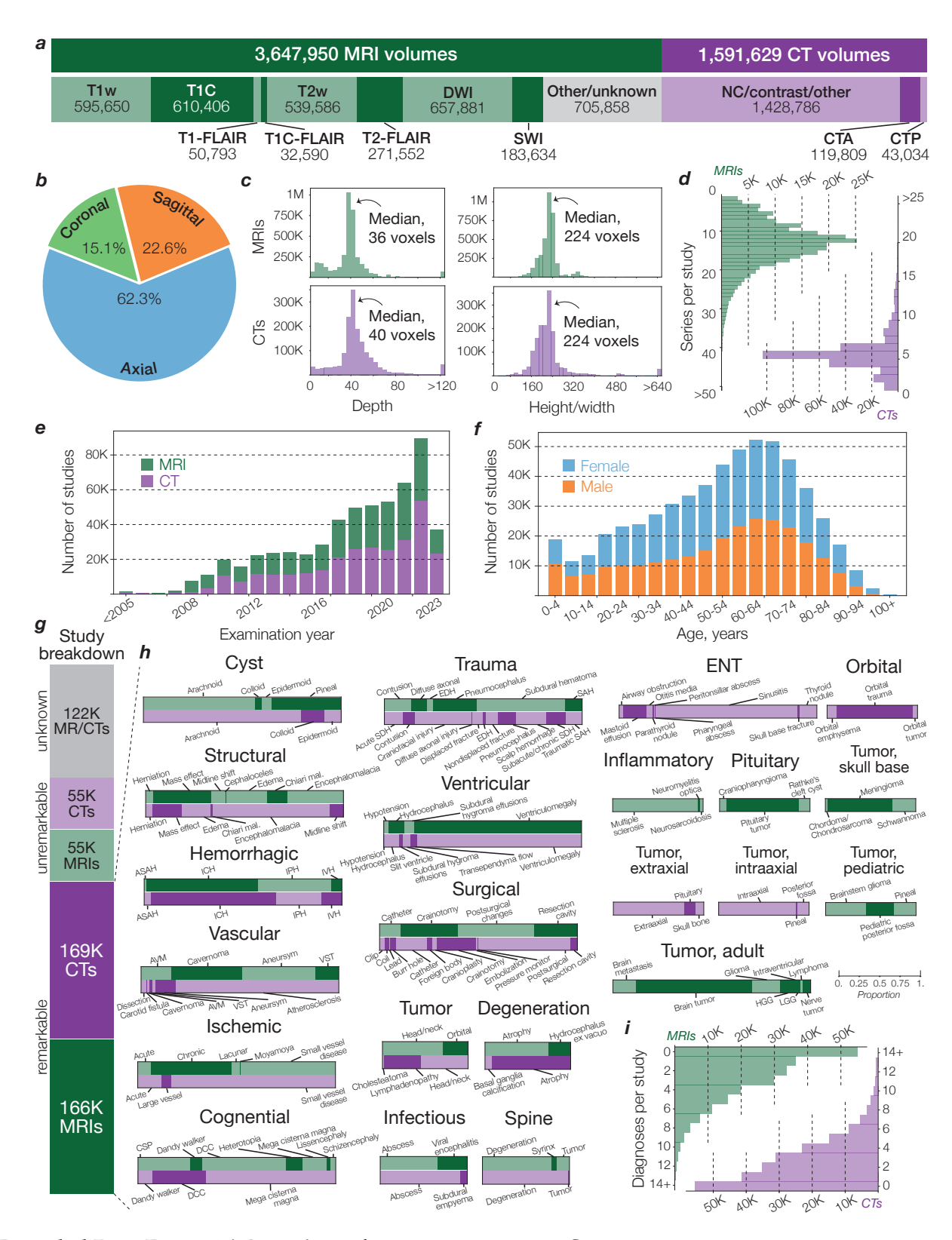
B.2. Supplementary Data Tables

- 1. Descriptive characteristics of the UM-NeuroImages prospective test set
- 2. Full task-level performance on the UM-NeuroImages CT test set
- 3. Full task-level performance on the UM-NeuroImages MRI test set
- 4. Performance of NeuroVFM on external neuroimaging benchmarks
- 5. Generated reports and evaluations for the UM-NeuroImages-Triage test set
- 6. Hyperparameters for NeuroVFM pretraining and UM-NeuroImages study-level attentive probing
- 7. Hyperparameters for NeuroVFM-LLaVA training and inference



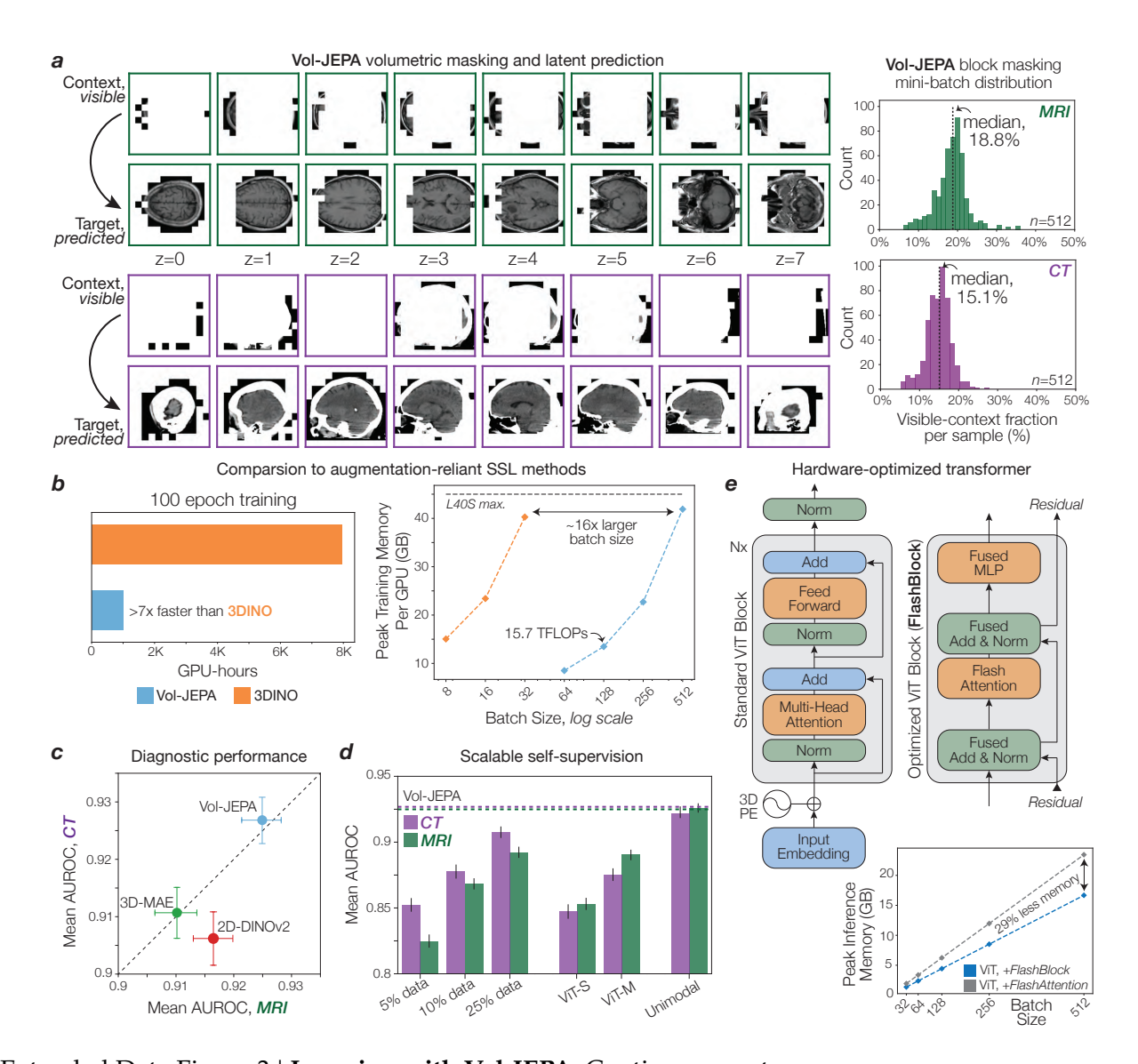
Extended Data Figure 1 | Extended NeuroVFM workflow. Caption on next page.

Extended Data Figure 1 | Extended NeuroVFM workflow. a, We queried the Michigan Medicine PACS for neuroimaging studies of the head, brain, face, orbits, and neck. After removing non-image and corrupted entries, the UM-NeuroImages cohort comprises 566,915 CT and MRI studies, of which 444,188 have paired radiology reports. Per-modality counts of volumes, studies, and reports are shown. To obtain training and evaluation labels at scale, we used an LLM report-parsing pipeline (7) that (1) extracts a list of expert-defined diagnoses and (2) converts free-text impressions to structured, itemized findings. Examples of both outputs are shown. b, Raw CT/MRI volumes are first resampled to $1 \times 1 \times 4$ mm (4 mm along the native acquisition axis) to reflect conventional clinical slice spacing. MRI intensities are clipped to 0.5-99.5th percentile, and CT volumes are windowed into brain, blood, and bone using standard Hounsfield windows. All volumes are quantized to 8-bit (CT blood/bone further reduced to 4-bit) to reduce footprint. Modality-specific foreground masks remove air only (no skull-stripping). The resulting dataset contains 11.8 billion 3D 4x16x16 patches (approximately 9 TB). c, Example CT/MRI volumes after background removal and tokenization. For Vol-JEPA training, volumes are partitioned into context-target pairs. Mask placements and lengths are randomized to cover diverse spatial configurations. d, In Vol-JEPA, a student volumetric transformer first encodes the context, after which a predictor combines these latents with the masked target positions to predict target latents. A teacher encoder (an EMA of the student) processes the full volume to produce target latents for the masked region. The objective minimizes the smooth L1 distance between the predicted and teacher target latents. Only the student and predictor receive gradients, and ultimately the student is used for downstream inference. e, To compare fairly across architectures, we use a unified study-level attentive probing strategy across all available tokens. 2D models (e.g., DINOv3 and BiomedCLIP) encode each slice, with classification, register, and patch tokens from all slices fed to the study-level probe. 3D volume-level models (e.g., NeuroVFM and VideoMAE) encode each volume, with all tokens pooled jointly. 3D study-level models (e.g., HLIP) natively output study classification tokens, but for parity we use all available output tokens in the study-level probe. f, We used NeuroVFM to condition a multimodal LLM in a LLaVa-1.5 style to generate preliminary neuroimaging findings. First, each volume in a study is encoded with frozen NeuroVFM. The resulting tokens are condensed by a per-volume Perceiver resampler to 64 latents. These then pass through the LLM connector (two-layer MLP) and are fed as vision tokens to a decoder-only LLM (e.g., Qwen3-14B). During finetuning, the clinical indication is given as text input and the model is trained to generate the itemized findings from a. An example indication and generated findings are shown. g, Illustrative deployment of NeuroVFM within a secure hospital environment. Each time a patient undergoes neuroimaging, an internal function call applies NeuroVFM to generate preliminary findings. An external state-of-the-art reasoning model receives only these findings (no images or PHI) to perform tasks such as triage and referral. Its output can then trigger service-line alerts (e.g., "page neurosurgery").



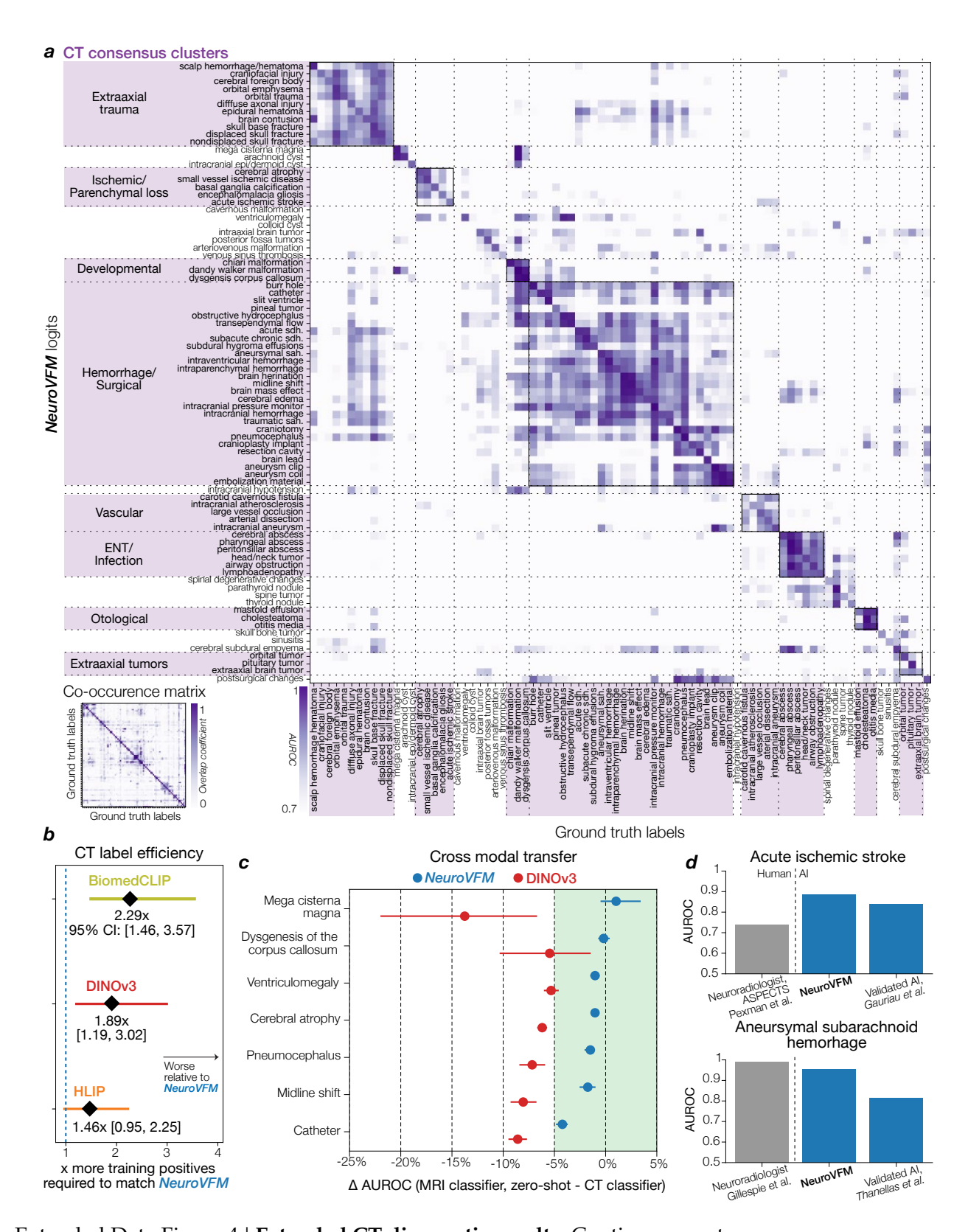
Extended Data Figure 2 | Overview of UM-NeuroImages. Caption on next page.

Extended Data Figure 2 | **Overview of UM-NeuroImages**. Descriptive statistics for the retrospective training corpus used for NeuroVFM. a, Volume counts by modality and sequence family. Sequence families were inferred from the DICOM "Series Description" via keyword matching. Counts are therefore approximate and may not perfectly reflect acquisition parameters. b, Distribution of volume orientation (axial, sagittal, coronal). c, Voxel-space distributions by modality: depth (slices) and in-plane dimension (height/width). Medians are indicated (MRI depth, 36 slices; CT depth, 40 slices; in-plane size for both, 224 voxels). d, Distribution of series per study by modality, showing a higher number of series in MRI (mode, 12) relative to CT (mode, 5). e, Study counts by calendar year (2005-2023) for MRI and CT. June 1, 2023 marks the cut-off for inclusion in the training set. f, Study counts by patient age (5-year bins) and sex. g, Breakdown of studies by label status: remarkable (at least 1 positive diagnosis), unremarkable (no reported abnormality), and unknown (no paired report). Totals shown correspond to 168,579 CT and 165,780 MRI remarkable studies; 55,444 CT and 55,051 MRI unremarkable studies; and 122,061 studies with no retrieved report used for Vol-JEPA self-supervised pretraining. h, Per-category prevalence of diagnoses (82 CT labels, 74 MRI labels). The aim was to design a clinically relevant ontology of diagnostic classes to evaluate our representation models. We refer to this benchmark as UM-NeuroBench. Abbreviations: Hemorrhagic – ASAH, aneurysmal subarachnoid hemorrhage; ICH, intracranial hemorrhage; IPH, intraparenchymal hemorrhage; IVH, intraventricular hemorrhage. Vascular – AVM, arteriovenous malformation; VST, venous sinus thrombosis. Congenital – CSP, cavum septum pellucidum; DCC, dysgenesis of the corpus callosum. Trauma – EDH, epidural hematoma; SAH, subarachnoid hemorrhage; SDH, subdural hematoma. Tumor, adult - HGG, high-grade glioma; LGG, low-grade glioma. i, Number of positive diagnoses per study by modality. The long-tailed, multi-label distribution underscores our label breadth and enables training strong multi-diagnostic classifiers.



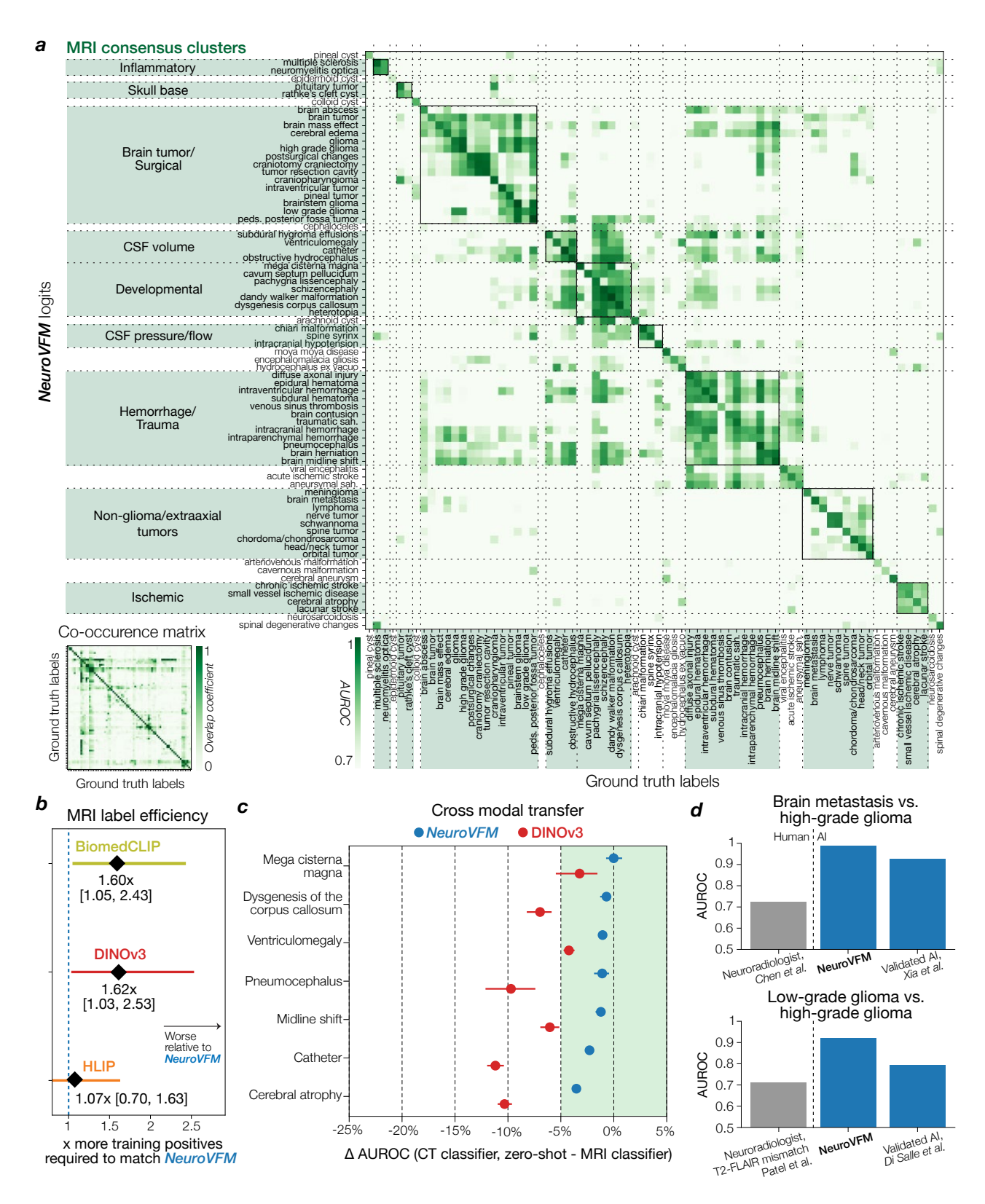
Extended Data Figure 3 | Learning with Vol-JEPA. Caption on next page.

Extended Data Figure 3 | Learning with Vol-JEPA. a, For each Vol-JEPA training instance, we generate context-target pairs by sampling (1) one or more large blocks whose union forms the masked target, or (2) a single small block that serves as the visible context. These blocks span all three axes, ensuring the encoder sees a diverse set of spatial volumes. Examples are shown for MRI and CT volumes across eight axial slices (z=0-7). **b**, Mini-batch histograms (n=512) show the per-instance visible-context fraction (MRI median, 18.8%; CT median, 15.1%). CT uses slightly smaller contexts because out-of-body voxels are reliably background. Since MRI foregrounds often include air due to lack of explicit skull stripping, we keep a slightly larger visible fraction to preserve anatomical signal. The range of fractions encourages the encoder to model shared neuroanatomy rather than background shortcuts. c, Robust volumetric self-supervised learning is typically expensive due to heavy augmentations and large forward passes. Left, a 3D-DINO-style baseline using MONAI 3D augmentations requires >7x GPU-hours than Vol-JEPA to train for 100 epochs. Right, peak training memory per GPU vs. batch size (log scale) shows Vol-JEPA encoding 16x larger batches for any given memory below the L40S limit. At batch size 128, throughput is approximately 15.7 TFLOPs/GPU. d, We trained a compute-matched VideoMAE (85% random masking) and DINOv2 on 2D images (UM-NeuroImages training corpus has 209M unique slices). Using the unified study-level attentive probing protocol (Extended Data Figure 1e), Vol-JEPA attains the highest mean AUROC on UM-NeuroBench for MRI and CT, indicating advantages of masked volumetric latent prediction over decoding-centric (VideoMAE) and 2D slice-only (DINOv2) approaches. e, We replaced the standard pre-norm ViT block (with FlashAttention-2) with a FlashAttention-2 block with operator fusion (Tri Dao, 2023). The schematic provided contrasts both implementations. Benchmarking demonstrated 29% lower peak inference memory used across batch sizes for ViT+FlashBlock vs. a standard ViT+FlashAttention stack, facilitating on-premises hospital deployment.



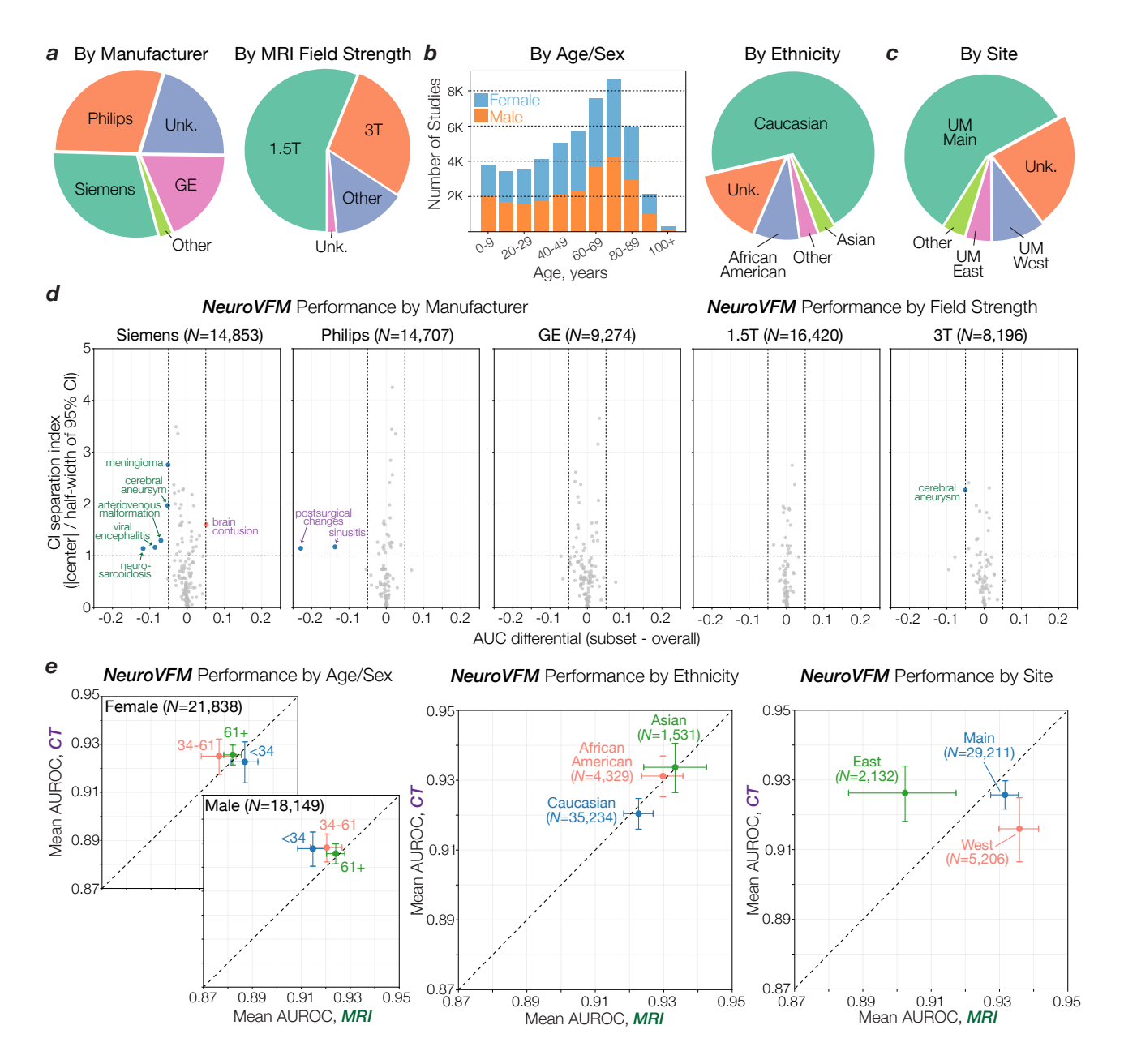
Extended Data Figure 4 | Extended CT diagnostic results. Caption on next page.

Extended Data Figure 4 | Extended CT diagnostic results. CT diagnostic evaluation comprises 82 diagnoses defined on UM-NeuroImages. All encoders were frozen and evaluated using the same study-level attentive probe (Extended Data Fig. 1e). a, Logit-label performance matrix for the NeuroVFM CT classifier, where each cell is AUROC of logit, against ground-truth label, (main diagonal shows per-diagnosis AUROC). Rows and columns are reorganized by hierarchical consensus clustering (bootstrapped similarity, average linkage). Lower left, reference co-occurrence matrix computed from ground truth using min-normalization, $M_{ij} = \frac{|i \cap j|}{\min(|i|, |j|)}$. **b**, Following the empirical scaling observed in Fig. 2e, we fit a shared slope across NeuroVFM and three baselines (BiomedCLIP, DINOv3, and HLIP) via ANCOVA ($p \ll 0.05$), relating calibrated F1 score to \log_{10} of the number of positive training instances. Intercept shifts yield data-equivalence factors (how many more positives a baseline requires to match NeuroVFM at a fixed F1), shown with 95% CIs. c, Cross-modal transfer results for seven diagnoses with shared semantics across MRI/CT. An MRI-trained classifier is evaluated zero-shot on CT, and we plot ΔAUROC = (MRI-on-CT) – (CT-on-CT) with 95% bootstrap CIs. For NeuroVFM, all differentials lie within the a priori equivalence band of ± 0.05 (green), whereas DINOv3 exhibits consistent modality shift. d, We compared NeuroVFM results on two representative CT detection tasks (top, acute ischemic stroke; bottom, aneurysmal subarachnoid hemorrhage) to published studies. NeuroVFM achieves AUROC comparable to expert neuroradiologists (14, 55) and to validated AI systems (56, 57). For prior studies, AUROC was approximated as the mean of the reported sensitivity and specificity.

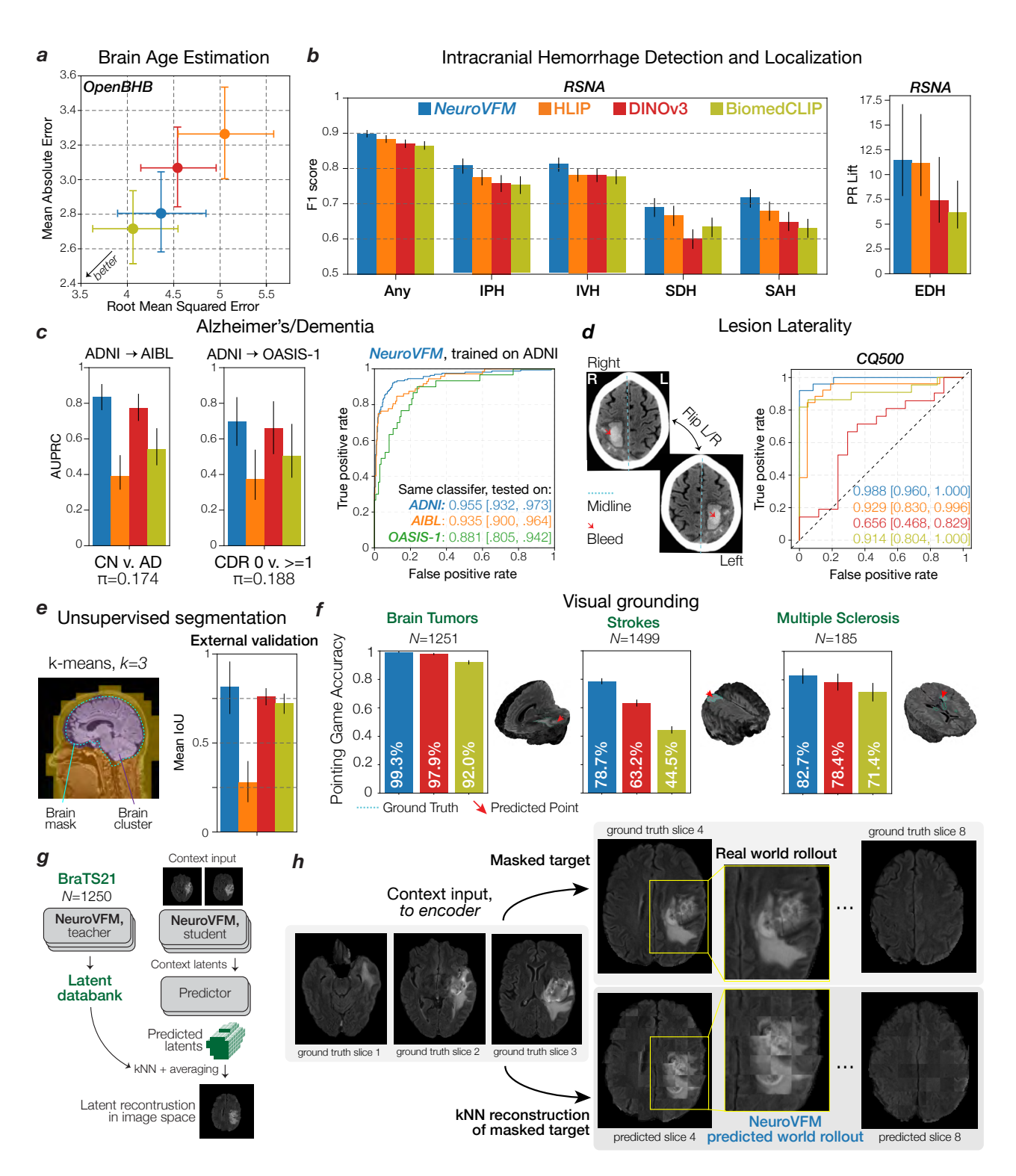


Extended Data Figure 5 | Extended MRI diagnostic results. Caption on next page.

Extended Data Figure 5 | Extended MRI diagnostic results. MRI diagnostic evaluation comprises 74 diagnoses defined on UM-NeuroImages. All encoders were frozen and evaluated using the same study-level attentive probe (Extended Data Fig. 1e). a, Logit-label performance matrix for the NeuroVFM MRI classifier, where each cell is AUROC of logit, against ground-truth label; (main diagonal shows per-diagnosis AUROC). Rows and columns are reorganized by hierarchical consensus clustering (bootstrapped similarity, average linkage). Lower left, reference co-occurrence matrix computed from ground truth using min-normalization, $M_{ij} = \frac{|i \cap j|}{\min(|i|, |j|)}$. **b**, Following the empirical scaling observed in Fig. 2e, we fit a shared slope across NeuroVFM and three baselines (BiomedCLIP, DINOv3, and HLIP) via ANCOVA ($p \ll 0.05$), relating calibrated F1 score to \log_{10} of the number of positive training instances. Intercept shifts yield data-equivalence factors (how many more positives a baseline requires to match NeuroVFM at a fixed F1), shown with 95% CIs. c, Cross-modal transfer results for seven diagnoses with shared semantics across MRI/CT. A CT-trained classifier is evaluated zero-shot on MRI, and we plot ΔAUROC = (CT-on-MRI) – (MRI-on-MRI) with 95% bootstrap CIs. For NeuroVFM, all differentials lie within the a priori equivalence band of ±0.05 (green), whereas DINOv3 exhibits consistent modality shift. d, We compared NeuroVFM results on two representative MRI differentiation tasks (top, brain metastasis vs. high-grade glioma; bottom, low- vs. high-grade glioma) to published studies. For NeuroVFM, the score was the pairwise logit margin (logit₁-logit₂), and AUROC was computed on this margin. NeuroVFM achieves AUROC comparable to expert neuroradiologists (15, 58) and to validated AI systems (59, 60). For prior studies that only report sensitivity and specificity, we approximate the AUROC as the average.

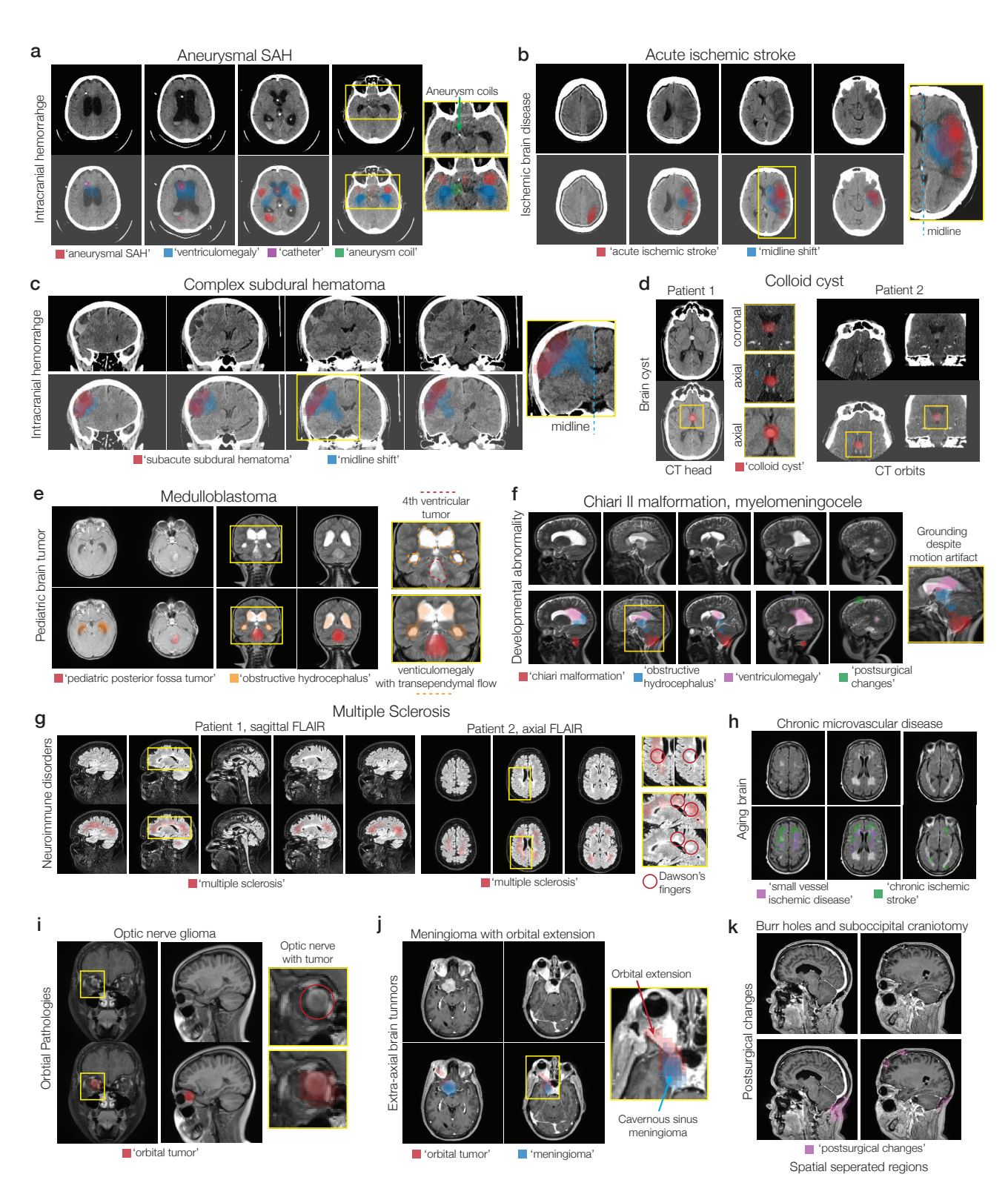


Extended Data Figure 6 | Subgroup and health system analysis. Descriptive statistics for the prospective testing corpus and robustness of NeuroVFM across common sources of health system variation. a, Composition by scanner manufacturer and MRI field strength. b, Composition by age/sex and ethnicity. c, Composition by acquisition site within the health system. We limited the analysis to the three most common sites: University of Michigan (UM) Main, West, and East. d, Per-diagnosis robustness checks by (left) manufacturer and (right) MRI field strength. For each eligible cell (subgroup × diagnosis; requires at least 10 positives and negatives present), we compute the AUC differential relative to the full test set ($\Delta_g = AUC_g - AUC_{all}$) using 10,000 paired, study-level bootstrap resamples to form percentile 95% CIs. Points show Δ_g , and the vertical dashed lines mark an a priori equivalence band of \pm 0.05 AUROC. The y-axis summarizes CI separation index, $S = \frac{\Delta_g}{\text{half-width}_{95\%}}$, where S > 1 indicates the 95% CI excludes 0 (i.e., a significant deviation). Cells with 95% CIs entirely within ± 0.05 AUROC were interpreted as showing no material deviation. Most diagnoses remain within the equivalence band, with outliers annotated (CT, purple; MRI, green). e, Mean AUROC (± 95% CIs) for MRI vs. CT stratified by age/sex, ethnicity, and site. No material differences present for age/sex and ethnicity. At the site level, MRI performance is lower at the East site, while CT is comparable across all.



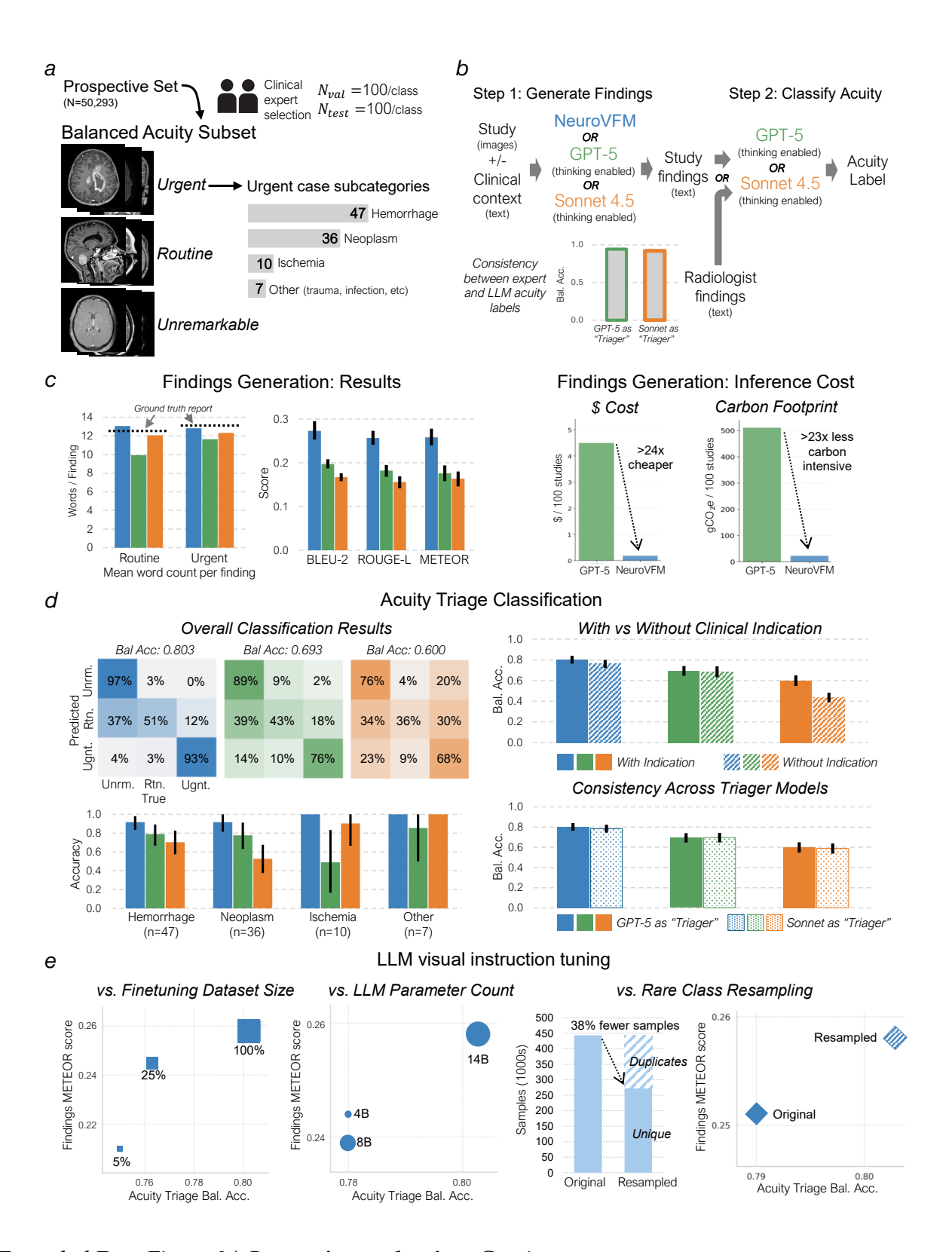
Extended Data Figure 7 | Open benchmarks performance. Caption on next page.

Extended Data Figure 7 | Open benchmarks performance. All encoders (NeuroVFM, blue; HLIP, orange; DINOv3, red; BiomedCLIP, olive) were frozen and evaluated using the same study-level attentive probe (Extended Data Fig. 1e). Error bars show 95% CIs. a, Brain age estimation results on the OpenBHB dataset (T1 MRIs). Scatter of RMSE (x-axis) vs. MAE (y-axis) per model shown. NeuroVFM is competitive (MAE, 2.805 years), second to BiomedCLIP. Strong 2D baselines likely benefit from dense slice-level features available to the probe. b, Intracranial hemorrhage detection and localization results on the 2019 RSNA-ICH dataset (non-contrast CT). Left, F1 for ICH detection and each subtype (IPH, IVH, SDH, SAH) shown. Right, PR lift for EDH (AUPRC/prevalence; EDH, 1.88%). NeuroVFM matches or exceeds other baselines across all tasks. c, We used three Alzheimer's/dementia cohorts to test whether features generalize beyond a single study: ADNI (training, with a held-out test set) and two independent test sets (AIBL and OASIS-1). ADNI to AIBL reflects classic domain shift, whereas ADNI to OASIS-1 probes robustness as OASIS-1 provides a dementia severity score (CDR 0 vs. ≥1). Left, training on ADNI and testing on AIBL/OASIS-1 yields strong AUPRC for NeuroVFM (DINOv3 comparable). Right, the same ADNI-trained NeuroVFM classifier exhibits high AUROC on the held-out ADNI test set and transfers well to AIBL and OASIS-1. These results indicate the learned NeuroVFM features capture disease-relevant information rather than site-specific cues, consistent with Fig. 3e where attention concentrates on structures known to be discriminative for Alzheimer's disease (18). d, Correct laterality assignment is clinically important yet rarely tested. The CQ500 dataset provides expert "Bleed-Left/Bleed-Right" labels, allowing a targeted laterality check given correct bleed detection. For each model, among studies it correctly flags as bleed, we horizontally flip the volume and measure changes in both the Bleed-Left and Bleed-Right logits (i.e., $\Delta_L = \text{logit}_L^{\text{flipped}} - \text{logit}_L$, $\Delta_R = \text{logit}_R^{\text{flipped}} - \text{logit}_R$). We summarize performance as AUROC over Δ_L and Δ_R against the ground-truth side. NeuroVFM is near perfect, representative of strong anatomical encoding. DINOv3, on the other hand, underperforms, plausibly due to strong flip-invariance from augmentations. e, K-means clustering (k=3) of dense patch embeddings from NeuroVFM yields coarse tissue-wise clusters that recover brain parenchyma without supervision. See Methods for full description. f, We quantitatively validated attention maps of models' UM-NeuroImages classifier against ground-truth segmentations on the BraTS21 ('brain tumor'), ATLAS v2.0 ('acute ischemic stroke'), and OpenMS ('multiple sclerosis') datasets. Specifically, we computed whether the voxel with the highest attention lies in the ground-truth segmentation, known as pointing game accuracy. Result and a representative example for each dataset are shown, with NeuroVFM demonstrating the highest degree of visual grounding. g, Schematic outlining how the predictor of NeuroVFM can be visualized via kNN reconstruction. To probe what the predictor infers for a masked target region, we project predicted latents back to image space via k-nearest-neighbor (kNN) retrieval. First, we build a patch latent databank by encoding patches from a reference set with the EMA teacher, yielding latent keys z_i and storing their corresponding image patches x_i . For a held-out volume, we encode a context region with the student encoder and use the predictor to produce latent predictions \hat{z}_i for each masked target patch. For each \hat{z}_i , we perform kNN search (cosine distance) over $\{z_i\}$, retrieve the top-k patches, and form a pseudo-reconstruction $\tilde{x}_j = \frac{1}{k} \sum_{i \in N_k} x_i$. h, Example rollout of a FLAIR volume from BraTS21. Here, three axial slices were passed to the student as context and the rest of the sequence was predicted and rolled out. Qualitatively, the reconstructions recover tumor extent and surrounding anatomy from the correct neuroimaging sequence and rollouts across adjacent slices maintain structural consistency, indicating that the predicted latents are accurate.



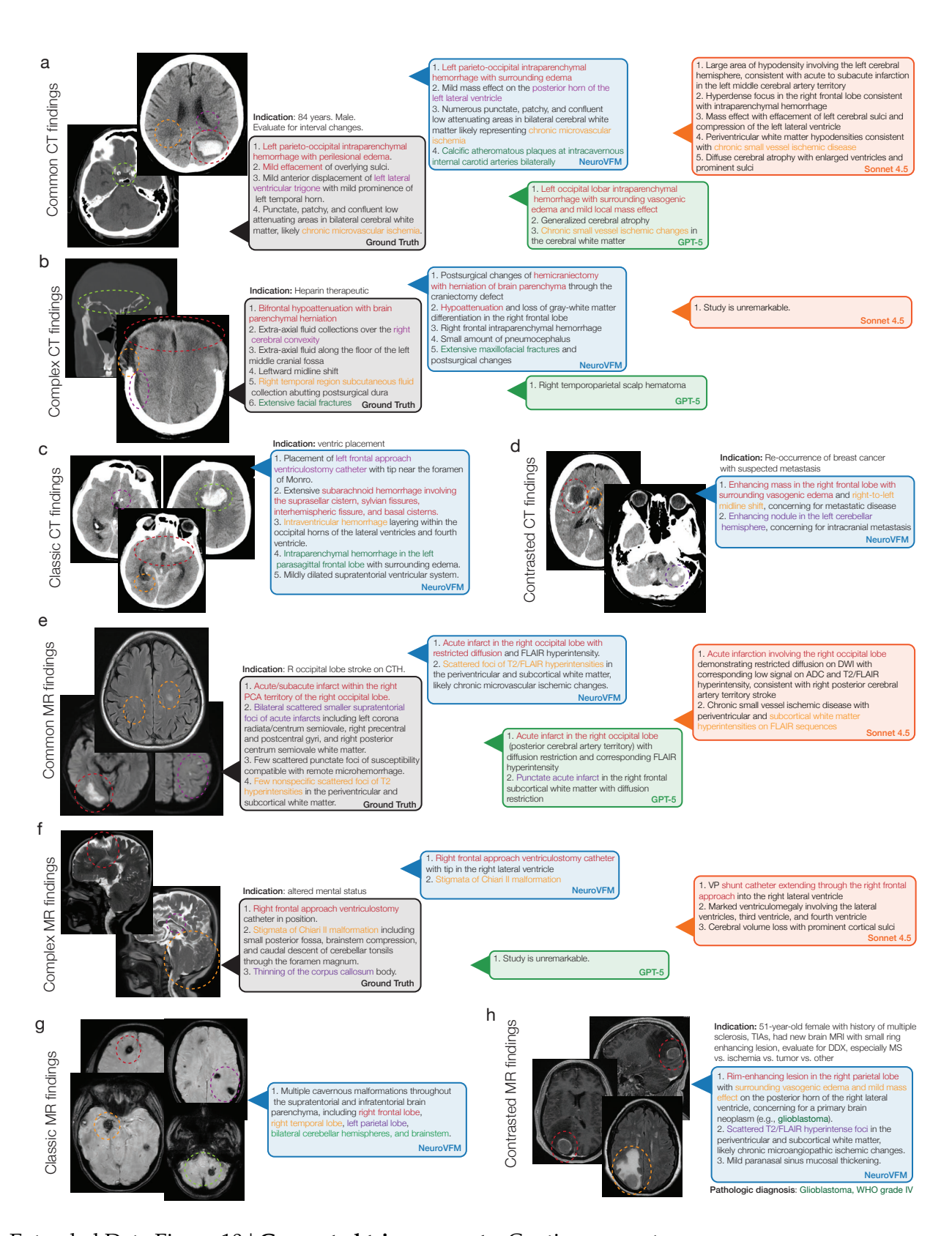
Extended Data Figure 8 | **Neuroimage scene understanding and grounded diagnoses.** Caption on next page.

Extended Data Figure 8 | Neuroimage scene understanding and grounded diagnoses. A diverse set of illustrative examples that demonstrate NeuroVFM is a grounded visual foundation model. a, An example of aneurysmal subarachnoid hemorrhage, treated via endovascular coiling, with associated hydrocephalus and ventricular catheter. NeuroVFM can parse the head CT into diagnostic regions and associate correct diagnoses. b, A patient with an acute middle cerebral artery ischemic stroke and associated cerebral edema and midline shift. c, A patient with a complex, septated, mixed-density subdural hematoma also causing midline shift. Note that NeuroVFM identifies midline shift regardless of the underlying etiology. d, Two patients with classic third ventricle colloid cysts. NeuroVFM attends to the colloid cyst regardless of patient orientation or imaging protocol. **e**, An example of a pediatric posterior fossa tumor causing obstructive hydrocephalus. NeuroVFM performs well across age groups. f, Example of a Chiari II malformation with associated obstructive hydrocephalus, ventriculomegaly, and previous cerebrospinal shunt placement. g, Two patients with newly diagnosed multiple sclerosis. Both patients have classic periventricular demyelination, known as Dawson's fingers, which NeuroVFM identifies on both sagittal and axial orientations. h NeuroVFM can differentiate between multiple sclerosis and periventricular white matter changes due to chronic microvascular disease. An example of an (i) optic nerve glioma and a (j) cavernous sinus meningioma with intraorbital extension. NeuroVFM performance generalizes well to ophthalmologic conditions. k, NeuroVFM can associate spatially separated regions, for example, surgeries completed in different locations, with the same underlying diagnosis. NeuroVFM can identify postsurgical changes throughout the neuroimaging study.



Extended Data Figure 9 | **Generative evaluation**. Caption on next page.

Extended Data Figure 9 | Generative evaluation. a, Composition of the 'UM-NeuroImages-Triage' evaluation dataset. The set consists of 600 studies (300 validation, 300 holdout) derived from our prospective test set. This set was hand-selected by neuroimaging experts to be balanced across three acuity classes ("Unremarkable", "Routine", "Urgent") and two modalities (MRI, CT). b, Schematic of the two-stage evaluation pipeline for neuroimaging report generation and clinical triage. Step 1 (Generate Findings): 3D studies (for NeuroVFM) or converted 2D slices (for GPT-5, Claude Sonnet 4.5) are provided to each model with a one-sentence clinical indication to generate key findings. Step 2 (Classify Acuity): The generated text is passed to an "LLM-as-a-judge" (Triager LLM: GPT-5 or Claude Sonnet 4.5) to classify the study into an acuity class. The pipeline was validated by passing ground-truth radiologist findings to the Triager LLMs, which achieved >94% accuracy in replicating the expert-designated acuity labels. c, Generated report quality and inference cost analysis. Left: Bar plots comparing NeuroVFM, GPT-5, and Claude Sonnet 4.5 on traditional NLP metrics (BLEU-2, ROUGE-L, METEOR) against ground-truth summarized reports. Right: Post-hoc analysis of inference efficiency, comparing dollar cost (USD) and carbon footprint (gCO2e) per 100 studies. NeuroVFM estimates assume inference on a single NVIDIA L40S GPU (AWS G6e instance) with a 3s/study inference time and southeast Michigan power grid intensity (0.5869 kgCO2e/kWh). GPT-5 estimates use October 2025 batch API pricing and carbon estimates from Jegham et al. (medium reasoning, >10k input/>1k output tokens) (61). d, Clinical triage accuracy and ablation studies. Top Left: Triage accuracy (3-class) of findings generated by NeuroVFM, GPT-5, and Claude Sonnet 4.5, evaluated by the "LLM-as-a-judge" pipeline. Bottom Left: Triage accuracy stratified by key acute pathologies (e.g., hemorrhage, aggressive mass, ischemia). Top Right: Ablation study on the impact of withholding the 1-sentence clinical indication from the input prompt. Bottom Right: Ablation study assessing the robustness of triage accuracy when using different "LLM-as-a-judge" models (GPT-5 vs. Claude Sonnet 4.5). e, Scaling properties of NeuroVFM visual instruction tuning. Left: Model performance (METEOR score and Triage Accuracy) as a function of finetuning training dataset size. Center: Model performance as a function of LLM parameter count (Qwen3-4B, 8B, 14B). Right: Comparison of model performance between the final model (trained on a dataset resampled based on diagnostic class rarity) and a baseline model trained on the original, imbalanced dataset, demonstrating the performance gains from data curation.



Extended Data Figure 10 | Generated triage reports. Caption on next page.

Extended Data Figure 10 | Generated triage reports. A diverse set of illustrative examples of generated triage reports. a, Example of a patient with a common lobar hemorrhage within the left parietal and occipital lobes. NeuroVFM and GPT-5 identified the hemorrhage and correctly localized it. **b**, A complex head CT of a patient who underwent a craniectomy after a traumatic brain injury. This example illustrates the challenge of interpreting real-world clinical neuroimaging studies that do not fit neatly into singular diagnoses, which is often observed in standardized research datasets. NeuroVFM was able to recognize the postsurgical and post-traumatic changes, while both GPT-5 and Claude Sonnet 4.5 were not able to interpret this image correctly. c, Classic subarachnoid hemorrhage pattern due to a ruptured anterior communicating artery aneurysm. d, Contrasted CTs are much less common. NeuroVFM was able to both recognize that this was a contrasted CT and interpret that the findings were most consistent with metastatic brain disease. e, A common example of restricted diffusion due to an acute infarct located in the right posterior cerebral artery (PCA) distribution. f, A complex patient with Chiari II malformation and myelomeningiocele. NeuroVFM was trained on pediatric MRIs with developmental abnormalities and is, therefore, able to correctly interpret this MRI. g, Classic appearance of cerebral cavernous malformations. h, A patient with a complex medical history and indication has a new brain lesion. NeuroVFM correctly identified this tumor as most likely a glioblastoma, confirmed on pathologic diagnosis.

SQL Query: Retrieve neuroimaging studies from PACS

```
USE "UMHS SDWH Datamodel";
GO

SELECT ExaminationDate, ExaminationInstitution, ExaminationAccessionNumber, ExaminationPatientId, ExaminationBodyPart,
ExaminationModality, ExaminationDescription, Patients.PatientPersonalld, Patients.PatientBirthdate, patients.PatientSex,
patients.PatientDeceased,Reports.ReportText, Reports.ReportDate

FROM dbo.Examinations INNER JOIN dbo.Patients ON Patients.PatientId = Examinations.ExaminationPatientId
inner join dbo.ExaminationReports on ExaminationReports.ExaminationReportExaminationId = Examinations.ExaminationId
inner join dbo.Reports on Reports.ReportId = ExaminationReports.ExaminationReportReportId

WHERE (Examinations.ExaminationBodyPart like "%Brain%" or Examinations.ExaminationBodyPart like "%Head%"
or Examinations.ExaminationDescription like "%Brain%" or Examinations.ExaminationDescription like "%Head%"
or Examinations.ExaminationDescription like "%Brain%" or Examinations.ExaminationDescription like "%Head%"
or Examinations.ExaminationDescription like "%Orbit%" or Examinations.ExaminationDescription like "%Neck%")
AND ExaminationS.ExaminationDate <= '2023-06-01 00:00:00'
```

Supplementary Data Figure 1 | **SQL query to retrieve neuroimaging studies**. Using the SDW, we retrieved all CT and MRI studies whose body part or description contained "brain," "head," "orbit(s)," or "neck," returning exam metadata and report text. The SQL query filters studies acquired before June 1 2023 for model development. The held-out prospective set applies the same query on and after that date.

Prompt: parse MRI diagnoses from report You, ChatGPT, are an expert neuroradiologist specializing in the interpretation of brain and spine MRI imaging reports. You will classify a radiology report according to the predefined list diagnoses below. This is a multilabel classification task, meaning a patient may have any number of these diagnoses (including none). Your job is to: 1. Parse the free-text radiology report. 2. Determine the presence or absence of each diagnosis based strictly on the imaging findings and/or impression sections. 3. Output a structured JSON object where: Each diagnosis is a key. - The value is an object with: - "rationale": A one-sentence explanation of the decision. - "label": "yes" if the diagnosis is present based on imaging findings and/or impression, "no" otherwise. Strict Classification Guidelines: - ONLY base the classification on the FINDINGS and IMPRESSION sections. - Ignore the INDICATION/HISTORY section unless it directly correlates with imaging findings. - A history of a condition does NOT mean it is present in the current imaging. - A diagnosis should be labeled "yes" only if explicitly stated in the imaging findings or mentioned as a possible diagnosis. - Example: "There is evidence of..." -> `"yes" - Example: "Findings are consistent with..." -> `"yes"` - Example: "Diagnoses on the differential are..." -> "yes" A diagnosis must be labeled `"no" if the report explicitly negates it or states it is resolved. Example: "No evidence of..." -> `"no"` - Example: "Previously resected..." -> `"no" - Example: "Normal exam, no abnormal findings..." -> `"no"` - If a condition is not mentioned at all in the findings/impression, classify it as "no" ** by default. - Example: If "brain metastasis" is not discussed in the findings, set "brain_metastasis": {"rationale": "No mention of brain metastasis in the findings.", "label": "no"}` - If the report states that there is no residual or no recurrence of a prior diagnosis, classify it as `"no"`. - Example: "No residual tumor seen." -> `"no"` - Example: "Prior infarct, but no acute ischemic stroke" -> `"acute_ischemic_stroke": "no" **Expected JSON Output Format** "subdural_hematoma": { "rationale": "No mention of subdural hematoma is present in the report.", "rationale": "The report explicitly states there is no epidural hematoma.", "label": "no" epidural_hematoma": { "encephalomalacia": { "rationale": "The report describes hypodense areas consistent with prior infarction, suggesting encephalomalacia.", "label": "yes" "rationale": "...", "label": "... Diagnoses List (Ensure a Key for Each in the JSON Output): <diagnoses, refer to caption>

Supplementary Data Figure 2 | MRI diagnosis extraction prompt. Caption on next page.

- Ensure strict adherence to the format (no missing brackets, misplaced commas, colons, or inconsistent tuple usage).

- Every diagnosis must have a key in the JSON output.

- Avoid free-text responses; only structured JSON format is allowed.

Supplementary Data Figure 2 | MRI diagnosis extraction prompt. We used an LLM-based annotation pipeline (7) with GPT-4.1-mini to convert free-text radiology reports into structured labels for 74 expert-defined MRI diagnoses. The prompt requires, for each diagnosis, a present/absent label and a brief rationale supporting the decision. The full list of MRI diagnoses is: subdural_hematoma; epidural_hematoma; brain_contusion; diffuse_axonal_injury; cerebral_aneurysm; arteriovenous_malformation; cavernous_malformation_cavernoma ("yes" if radiologist confident for cavernoma; "no" if possible microbleed); venous_sinus_thrombosis; acute_ischemic_stroke ("yes" for acute ischemia/infarct with diffusion restriction); chronic_ischemic_stroke ("yes" for chronic or evolving ischemia/infarct without diffusion restriction); moya_moya_disease; small vessel ischemic disease (also known as microvascular ischemic disease); lacunar stroke; intracranial_hemorrhage ("yes" for any intracranial hemorrhage, excluding microhemorrhage); intraparenchymal hemorrhage ("yes" for hemorrhages within the brain, usually spontaneous and due to hypertension); intraventricular_hemorrhage; aneurysmal_subarachnoid_hemorrhage ("yes" if due to ruptured aneurysm or other vascular cause); traumatic_subarachnoid_hemorrhage ("yes" if due to head trauma); multiple_sclerosis; neuromyelitis_optica; neurosarcoidosis; brain_abscess ("yes" if radiologist is confident for brain abscesses or subdural empyemas); viral encephalitis (most commonly herpes encephalitis involving the temporal and frontal lobes); arachnoid_cyst; pineal_cyst; epidermoid_cyst ("yes" for intracranial epidermoid cyst only); colloid_cyst; brain_tumor ("yes" for any intracranial mass, growth, or neoplasm); orbital_tumor ("yes" for any orbital mass, growth, or neoplasm); head_neck_tumor ("yes" for tumor/cancer in the oral cavity, throat, larynx, nasal cavity, salivary, and thyroid gland); spine_tumor ("yes" for any spine mass, growth, or neoplasm); nerve_tumor ("yes" for nerve, nerve root, or nerve sheath tumors); spinal_degenerative_changes; glioma ("yes" if mostly likely primary glial tumor); high_grade_glioma ("yes" if MRI features for high-grade glioma); low_grade_glioma ("yes" if MRI features for low-grade glioma); brain_metastasis; meningioma; schwannoma; lymphoma; pineal_tumor ("yes" for any tumor in the pineal region); intraventricular_tumor; pediatric_posterior_fossa_tumor (diagnosis includes, but not limited to, medulloblastoma, ependymoma, pilocytic astrocytoma); brainstem_glioma (diagnosis also called diffuse midline gliomas); pituitary_tumor; rathkes_cleft_cyst; craniopharyngioma; chordoma_chondrosarcoma; chiari_malformation ("yes" for chiari I/II malformations); cerebral_atrophy; brain_herniation; brain_mass_effect; brain_midline_shift; cephaloceles; encephalomalacia_gliosis; cerebral_edema; cavum_septum_pellucidum; dandy_walker_malformation; mega_cisterna_magna; heterotopia; pachygyria_lissencephaly; schizencephaly; dysgenesis_corpus_callosum; ventriculomegaly ("yes" for any abnormally enlarged ventricles); hydrocephalus_ex_vacuo ("yes" for ventriculomegaly due to brain atrophy, normal pressure hydrocephalus, or ex vacuo dilation); obstructive_hydrocephalus ("yes" for ventriculomegaly due to mass lesion or aqueductal stenosis); subdural_hygroma_effusions; intracranial_hypotension; craniotomy_craniectomy; tumor_resection_cavity; postsurgical_changes; pneumocephalus; catheter ("yes" for any intracranial catheter); spine_syrinx.

Prompt: parse CT diagnoses from report You, ChatGPT, are an expert neuroradiologist specializing in the interpretation of brain and spine CT imaging reports. You will classify a radiology report according to the predefined list diagnoses below. This is a multilabel classification task, meaning a patient may have any number of these diagnoses (including none). Your job is to: 1. Parse the free-text radiology report. 2. Determine the presence or absence of each diagnosis based strictly on the imaging findings and/or impression sections. 3. Output a structured JSON object where: Each diagnosis is a key. - The value is an object with: - "rationale": A one-sentence explanation of the decision. - "label": "yes" if the diagnosis is present based on imaging findings and/or impression, "no" otherwise. Strict Classification Guidelines: - ONLY base the classification on the FINDINGS and IMPRESSION sections. - Ignore the INDICATION/HISTORY section unless it directly correlates with imaging findings. - A history of a condition does NOT mean it is present in the current imaging. - A diagnosis should be labeled "yes" only if explicitly stated in the imaging findings or mentioned as a possible diagnosis. - Example: "There is evidence of..." -> `"yes" - Example: "Findings are consistent with..." -> `"yes"` - Example: "Diagnoses on the differential are..." -> "yes" A diagnosis must be labeled `"no" if the report explicitly negates it or states it is resolved. Example: "No evidence of..." -> `"no"` - Example: "Previously resected..." -> `"no" - Example: "Normal exam, no abnormal findings..." -> `"no"` - If a condition is not mentioned at all in the findings/impression, classify it as "no"*** by default. - Example: If "brain metastasis" is not discussed in the findings, set `"brain_metastasis": {"rationale": "No mention of brain metastasis in the findings.", "label": "no"}` - If the report states that there is no residual or no recurrence of a prior diagnosis, classify it as `"no"`. - Example: "No residual tumor seen." -> `"no"` - Example: "Prior infarct, but no acute ischemic stroke" -> `"acute_ischemic_stroke": "no"` **Expected JSON Output Format** "acute_subdural_hematoma": { "rationale": "No mention of acute subdural hematoma is present in the report.", "rationale": "The report explicitly states there is no epidural hematoma.", "label": "no" epidural_hematoma": { "encephalomalacia": { "rationale": "The report describes hypodense areas consistent with prior infarction, suggesting encephalomalacia.", "label": "yes" "rationale": "...", "label": "... Diagnoses List (Ensure a Key for Each in the JSON Output):

Supplementary Data Figure 3 | CT diagnosis extraction prompt. Caption on next page.

- Ensure strict adherence to the format (no missing brackets, misplaced commas, colons, or inconsistent tuple usage).

<diagnoses, refer to caption>

- Every diagnosis must have a key in the JSON output.

- Avoid free-text responses; only structured JSON format is allowed.

Supplementary Data Figure 3 | CT diagnosis extraction prompt. We used an LLM-based annotation pipeline (7) with GPT-4.1-mini to convert free-text radiology reports into structured labels for 82 expert-defined CT diagnoses. The prompt requires, for each diagnosis, a present/absent label and a brief rationale supporting the decision. The full list of CT diagnoses is here: acute_subdural_hematoma ("yes" if acute blood in subdural space, often after head trauma and associated with midline shift); subacute_chronic_subdural_hematoma ("yes" if subacute or chronic blood in the subdural space, often non-traumatic); epidural_hematoma; brain_contusion; displaced_skull_fracture ("yes" if displaced or depressed skull fracture); nondisplaced_skull_fracture; skull_base_fracture; orbital_trauma ("yes" if orbit fracture, globe rupture, or other orbital trauma); orbital_emphysema; pneumocephalus; diffuse_axonal_injury; craniofacial_injury ("yes" if any mandibular, maxillary, zygoma, or other facial fractures or trauma); intracranial_hemorrhage ("yes" any intracranial hemorrhage); intraparenchymal_hemorrhage ("yes" for hemorrhages within the brain, usually spontaneous and due to hypertension); aneurysmal_subarachnoid_hemorrhage ("yes" if due to ruptured aneurysm or other vascular cause); traumatic_subarachnoid_hemorrhage ("yes" if due to head trauma); intraventricular hemorrhage; scalp hemorrhage hematoma; acute_ischemic_stroke ("yes" for acute ischemia/infarct often with cerebral edema, mass effect, midline shift); small_vessel_ischemic_disease (also known as microvascular ischemic disease); large_vessel_occlusion ("yes" if large-vessel occlusion found on CT angiogram); intracranial_atherosclerosis; arterial_dissection ("yes" if dissection found on CT angiography); carotid cavernous_fistula; cerebral_venous_sinus_thrombosis ("yes" if thrombosis found on CT angiogram/venogram); intracranial_aneurysm ("yes" if found on CT angiogram); cavernous_malformation_cavernoma ("yes" if radiologist confident for cavernoma; "no" if possible microbleed); cerebral_arteriovenous_malformation; intra_axial_brain_tumor ("yes" for tumors within the brain parenchyma); extra_axial_brain_tumor ("yes" for tumors outside the brain parenchyma, but inside the skull/intracranial space); orbital_tumor ("yes" if diagnosis of any orbital mass, growth, or neoplasm); pineal_tumor ("yes" for any tumor in the pineal region); pituitary_tumor; skull bone tumor; posterior fossa tumors ("yes" for any tumor in the posterior fossa, cerebellum, or brainstem); head_neck_tumor ("yes" if diagnosis of tumor/cancer in the oral cavity, throat, larynx, nasal cavity, salivary, and thyroid gland); spine_tumor ("yes" if diagnosis of any spine mass, growth, or neoplasm); spinal_degenerative_changes; arachnoid_cyst; intracranial_epidermoid_dermoid_cyst; colloid_cyst; cerebral_subdural_empyema; cerebral_abscess; craniotomy; cranioplasty_implant ("yes" if artificial implant to repair skull defect); burr hole; resection cavity; postsurgical changes; catheter ("yes" for any intracranial catheter); intracranial_pressure_monitor; brain_lead ("yes" for brain electrode leads used in functional neurosurgery); aneurysm_coil; aneurysm_clip; embolization_material; cerebral_foreign_body (examples include glass, metal, plastic, wood); ventriculomegaly; obstructive_hydrocephalus; transependymal_flow; subdural_hygroma_effusions; slit_ventricle; intracranial_hypotension; cerebral_edema; cerebral_atrophy; brain_herniation; brain_mass_effect; midline_shift; encephalomalacia_gliosis; basal_ganglia_calcification; chiari_malformation ("yes" for Chiari I/II malformations); dysgenesis_corpus_callosum; dandy_walker_malformation; mega_cisterna_magna; sinusitis; mastoid_effusion (includes mastoid fluid and mastoiditis); otitis_media; peritonsillar_abscess; pharyngeal_abscess (includes retropharyngeal and parapharyngeal abscesses); cholesteatoma; head_neck_enlarged_lymph_node; airway_obstruction (examples include septal deviation, choanal atresia, obstruction, airway edema, laryngeal edema, and pharyngeal edema); thyroid nodule; parathyroid nodule.

Step 1: Summarize findings from report

Your task is to shorten MRI reports by summarizing abnormalities and removing certain information. Please summarize the abnormalities in the report above in an one-level enumerated list without indents. Only include abnormalities. Your summarization must not include items that are normal or not evident (like "No ...", or "No evidence of ...", or "Normal ..." or "Unremarkable ..."). If there is no abnormalities in this report, write "1. Study is unremarkable."

Step 2: Remove unremarkable statements

Your goal is to modify a list of radiology findings with the following rules:

- 1. Remove all the items in the list that are fully normal (i.e. items that indicates something is normal or unremarkable, or nothing special is found, or no evidence or nothing significant). Write "<Removed>" for the removed items.
- 2. If an item in the list contains both normal and abnormal information, only remove the normal parts. Keep the abnormal parts in the item, and do not delete the item. Make sure you remove sentences staring with "No ..." or "Unremarkable ...".
- 3. Please also remove all phrases that contain "clinical correlation" or suggestions for further evaluation with additional studies (such as recommending future MRIs).
- 4. Do not remove other abnormal information unless specified above. Do not remove benign abnormalities.

Step 3: Remove comparisons to prior studies and measurements

Your goal is to modify a list of radiology findings with the following rules:

- 1. Remove all phrases that indicates a comparison to a previous report, such as redemonstration, stable, stable in comparison, unchanged, compared to, prior exam, interval improvement, interval worsening, interval increase, interval reduction, old, increase in size, reduction in size, etc.
- 2. Please also remove all numerical size measurements, such as "8 mm" or "3 cm". Do not remove non-numerical description of size, such as "small", "minimal" or "large".
- 3. Please remove all date phrases such as "06/20/2012" from all items.\n\n4. Please remove all references to patient history, such as "compatible with history of ..."

Your output should have the same number of rows as the input.

Supplementary Data Figure 4 | **Prompts for structured findings extraction.** Three successive prompts were applied to GPT-4.1-mini to turn free-text radiology reports into an itemized list of structured findings for report generation. The pipeline extracts key positive findings and removes unremarkable statements, comparisons to prior studies, and raw measurements. The resulting findings supervised training of NeuroVFM-LLaVA for preliminary findings generation.

Prompt: Generate findings given neuroimaging study and clinical indication

```
# Objective:
 Analyze the provided neuroimaging study, using the provided clinical indication to inform your analysis, and generate a structured findings
 report as a single JSON object.
 Assess the images and list all relevant radiological findings, using the Findings List Guidelines below. NOTE: The provided images are
cross-sectional slices from one or more 3D scans from the study. **Images are presented in radiological orientation, where the LEFT side
of the image corresponds to the RIGHT side of the patient.**
 # Findings List Guidelines:
 - **Analyze the Provided Images Only:** All findings must be based on the provided image only. Do NOT make statements that imply
comparison to a prior study (e.g., 'stable/progressing', 'growing/shrinking').

- **Include Significant Pertinent Positives:** The list must only contain statements about the existence of abnormal, clinically significant
findings. If there are no abnormal findings, you must include a single item in the list "Study is unremarkable."

- **Exclude Negative/Normal Findings:** Do **not** include statements about the absence of a pathology (e.g., 'no hemorrhage') or
 statements about normalcy of structures (e.g., 'ventricles are normal').
 - **Direct Language:** Rewrite findings as direct anatomical descriptions. Remove introductory phrases.
 # Output Format
 - Your response must consist of ONLY a single JSON object with a single field "findings", which should be a list of strings
  "findings": [
Now, analyze the following neuroimaging study in the context of the given indication.
```

Supplementary Data Figure 5 | **Frontier model prompt for study findings.** To assess reasoning models (e.g., GPT-5-thinking) on preliminary neuroimaging findings generation, we passed the clinical indication and the study slice-by-slice. The prompt asks for an itemized list of key findings at the study level.

Prompt: Assign triage level given findings and indication

```
Analyze the provided list of radiological findings from a neuroimaging study, using the provided clinical indication to inform your
analysis, and generate a clinical triage analysis as a single JSON object.
 1. Assess: Write a single, concise "triage_assessment" sentence which explains the clinical acuity of the patient's condition based
on the provided findings. Your assessment should be based ONLY on this text. Do not infer any information not present in the list.
2. Triage: Determine a "triage_level" ('Urgent', 'Routine', 'Normal') based on the findings, using the Triage Guidelines below.
 # Triage Guidelines:
 - **Urgent**: A study is classified as 'Urgent' if it contains any new or worsening findings that require immediate clinical attention to
 prevent significant harm.
  **Routine**: A study is classified as 'Routine' if it contains any notable findings that may require medical follow-up but are NOT
 immediately life-threatening. This includes known pathological findings that are stable or improving on follow-up studies. Only
 select Routine if the case REQUIRES specific clinical followup.
 - **Normal**: A study is classified as 'Normal' if it is grossly unremarkable and does NOT require ANY clinical follow-up. Mild
 mucosal thickening, mild chronic microvascular changes, mild calcifications, or mild cerebral volume loss are all considered Normal.
 - **Examples of Urgent Findings:** (NON-exhaustive list meant to guide decision making)
  - Acute intracranial hemorrhage (e.g., subarachnoid, subdural, epidural, intraparenchymal)
  - Traumatic injury: Skull fractures (especially depressed or crossing vascular structures) or significant intracranial air (pneumocephalus)
  - Acute spinal column or cord injury: Vertebral fracture with subluxation, epidural hematoma, or severe cord compression
  - Signs of brain herniation or significant mass effect
  - Severe hydrocephalus or ventriculomegaly
  - Acute ischemic infarct (e.g., loss of grey-white differentiation, dense vessel sign) or large vessel occlusion on CT Angiography
  - Acute vascular injury, such as arterial dissection
  - Acute venous sinus thrombosis
  - Features of an aggressive mass (e.g., destructive bone lesion, ring-enhancing mass)
  - Features of severe infection (e.g., cerebral abscess, ventriculitis, encephalitis, epidural abscess)
 # Output Format
 - JSON object with 2 fields:
  "triage_assessment": "...",
  "triage_level": "Normal/Routine/Urgent",
Now, synthesize the given radiological findings and clinical indication into a triage assessment.
```

Supplementary Data Figure 6 | **Triage prompt given findings and indication.** Using a standardized protocol, we supply the clinical indication and itemized findings to a reasoning model (e.g., GPT-5-thinking) and request a single triage label with a brief justification. Labels are drawn from an expert-defined schema aligned with routine clinical triage. When provided ground-truth reports, both models show high accuracy and close agreement with clinician labels (Extended Data Fig. 9b), supporting the validity of their reasoning.

Supplementary Data Table 1 | **Descriptive characteristics of the UM-NeuroImages prospective test set.** The temporally held-out UM-NeuroImages test set comprises 50,293 CT and MRI studies. For each study, the table reports modality, scanner manufacturer, acquisition site, patient age at scan (with ages >90 years truncated to 90 years due to PHI constraints), sex, ethnicity, and MRI field strength (when applicable). *This large table is available in the accompanying spreadsheet*.

Supplementary Data Table 2 | Full task-level performance on the UM-NeuroImages CT test set. The temporally held-out UM-NeuroImages CT test set comprises 21,054 CT studies with 82 study-level CT diagnoses. For each diagnosis and diagnostic category, the table reports the classification performance of NeuroVFM and three baseline models (HLIP, DINOv3, and BiomedCLIP). This large table is available in the accompanying spreadsheet.

Supplementary Data Table 3 | **Full task-level performance on the UM-NeuroImages MRI test set.** The temporally held-out UM-NeuroImages MRI test set comprises 29,239 MRI studies with 74 study-level MRI diagnoses. For each diagnosis and diagnostic category, the table reports the classification performance of NeuroVFM and three baseline models (HLIP, DINOv3, and BiomedCLIP). *This large table is available in the accompanying spreadsheet.*

Supplementary Data Table 4 | **Performance of NeuroVFM on external neuroimaging benchmarks.** The table summarizes the performance of NeuroVFM and three baseline models (HLIP, DINOv3, and BiomedCLIP) on eight external neuroimaging benchmarks (six MRI and two CT datasets). All models were evaluated using 8-fold stratified cross-validation with a 20% held-out test split, except for AIBL and OASIS-1, which were evaluated on the entire dataset using the ADNI-trained classifier. *This large table is available in the accompanying spreadsheet*.

Supplementary Data Table 5 | **Generated reports and evaluations for the UM-NeuroImages-Triage test set.** For the balanced UM-NeuroImages-Triage test set of 300 studies, the table includes generated reports from all models, the corresponding ground-truth radiology reports, clinical indication, triage labels, and all associated evaluation scores from expert raters. *This large table is available in the accompanying spreadsheet*.

Supplementary Data Table 6 | **Hyperparameters for NeuroVFM pretraining and UM-NeuroImages study-level attentive probing.** The table lists all hyperparameters used to (1) pretrain the 3D ViT backbone and (2) train the study-level attentive probe used for UM-NeuroImages. For each configuration, we report optimization settings, data sampling strategies, architectural choices, and regularization parameters. A similar probing strategy was used for all external benchmarks, with hyperparameters adjusted for dataset size and complexity. *This large table is available in the accompanying spreadsheet.*

Supplementary Data Table 7 | **Hyperparameters for NeuroVFM-LLaVA training and inference.** The table lists all hyperparameters used to perform LLaVA-1.5-style vision-instruction tuning on top of the frozen NeuroVFM backbone to finetune a language model for key findings generation. Reported settings include model initialization, optimizer configuration, learning rate schedule, batch size, context length, training duration, and inference parameters. The deployed inference pipeline is implemented with HuggingFace to enable standardized report generation. *This large table is available in the accompanying spreadsheet*.